



Generation of large-scale gravity waves and neutral winds in the thermosphere from the dissipation of convectively generated gravity waves

Sharon L. Vadas¹ and Han-li Liu²

Received 29 January 2009; accepted 11 June 2009; published 21 October 2009.

[1] We study the response of the thermosphere and ionosphere to the dissipation of gravity waves (GWs) excited by a deep convective plume on 1 October 2005 at 52.5°W, 15.0°S, and 2120 UT in Brazil. Those small- and medium-scale GWs which reach the thermosphere dissipate at $z \sim 120\text{--}250$ km in a direction opposite to the background wind $\sim(1\text{--}2)$ density scale heights below. This localized momentum deposition creates horizontal thermospheric body forces that have large sizes and amplitudes and generates large-scale secondary GWs and large-scale traveling ionospheric disturbances (LSTIDs) that propagate globally away from the body force in all directions except that perpendicular to the force direction. For the convective plume at 2120 UT, the secondary GWs have horizontal wavelengths of $\lambda_H \sim 2100\text{--}2200$ km, periods of $\tau_r \sim 80$ min, horizontal phase speeds of $c_H \sim 480\text{--}510$ m/s, density perturbations as large as $|\rho'/\bar{\rho}| \sim 3.6\text{--}5\%$ at $z = 400$ km, relative [O] perturbations as large as $\sim 2\text{--}2.5\%$ at $z = 300$ km, and total electron content perturbations as large as $\sim 8\%$. This transfer of momentum from local, relatively slow, small scales at the tropopause to global, fast, large scales in the thermosphere is independent of geomagnetic conditions. The various characteristics of these large-scale waves may explain observations of LSTIDs at magnetically quiet times. We also find that this body force creates a localized “mean” horizontal wind in the direction of the body force. For the plume at 2120 UT, the wind is southward with an estimated maximum of $v_{\max} \sim -400$ m s⁻¹ that is dissipated after ~ 4 h. We also find that the induced body force direction varies throughout the day, depending on the winds in the lower thermosphere.

Citation: Vadas, S. L., and H. Liu (2009), Generation of large-scale gravity waves and neutral winds in the thermosphere from the dissipation of convectively generated gravity waves, *J. Geophys. Res.*, *114*, A10310, doi:10.1029/2009JA014108.

1. Introduction

[2] When the troposphere is convectively unstable, moist air can rise quickly to the tropopause within localized convective updrafts. If energetic enough, these plumes can push into the stably stratified stratosphere and excite gravity waves (GWs) [Alexander *et al.*, 1995; Holton and Alexander, 1999; Lane *et al.*, 2001, 2003; Piani *et al.*, 2000; Horinouchi *et al.*, 2002; Vadas and Fritts, 2009 (hereinafter VF2009)]. Those GWs with large phase speeds can avoid mean wind critical level filtering [Hines and Reddy, 1967], and those GWs with small amplitudes can avoid wave breaking in the lower atmosphere and can propagate into the thermosphere [Fritts and Alexander, 2003]. In the ionosphere, propagating neutral GWs push and pull plasma along the Earth's

magnetic field lines, which causes periodic advection and compression of the plasma called traveling ionospheric disturbances (TIDs) [e.g., Hocke and Schlegel, 1996]. Many studies have correlated medium-scale TIDs (MSTIDs) and ionospheric irregularities with convectively unstable sources such as convection, hurricanes, and tornados [Bauer, 1958; Georges, 1968; Röttger, 1977; Hung *et al.*, 1978; Hung and Kuo, 1978; Hung and Smith, 1978; Waldoock and Jones, 1987; Kelley, 1997; Hocke and Tsuda, 2001; Bishop *et al.*, 2006].

[3] A GW's amplitude grows nearly exponentially with altitude, because of the decreasing background density. In the thermosphere, GWs are subject to dissipative processes such as kinematic viscosity, thermal diffusivity, ion drag, wave-induced diffusion, and nonlinear wave interactions [Pitteway and Hines, 1963; Hines and Hooke, 1970; Francis, 1973; Gossard and Hooke, 1975; Richmond, 1978; Del Genio and Schubert, 1979; Maeda, 1985; Vadas and Fritts, 2005 (hereinafter VF2005); Miyoshi and Fujiwara, 2008; Yigit *et al.*, 2008]. Those GWs propagating against the background wind propagate to higher altitudes than those propagating in the same direction as the wind [Hines and Reddy, 1967; Cowling *et al.*, 1971; Waldoock and Jones, 1984,

¹CoRA Division, NorthWest Research Associates, Boulder, Colorado, USA.

²High Altitude Observatory, National Center for Atmospheric Research, Boulder, Colorado, USA.

1986; *Crowley et al.*, 1987; *Fritts and Vadas*, 2008 (hereinafter FV2008); *Miyoshi and Fujiwara*, 2008]. Because of dissipative filtering, those waves propagating perpendicular to the wind direction do not reach the highest altitudes, as was previously thought [*Cowling et al.*, 1971].

[4] When a GW dissipates, it causes momentum flux divergence and induces a horizontal acceleration of the background neutral wind in the direction that it was propagating [e.g., *Fritts and Alexander*, 2003]. Employing an idealistic stratospheric shear, the localized thermospheric body force which resulted from GWs excited from a single deep convective plume was calculated to have full zonal and meridional widths and depths of $\sim 600 \text{ km} \times 600 \text{ km} \times 40\text{--}80 \text{ km}$ in the x , y , and z directions, respectively, and to last for 0.5–1 h [*Vadas and Fritts*, 2006] (hereinafter VF2006). The amplitude of the body force, however, was uncertain because of the simplicity of the wind and temperature model used, and was estimated to be $\simeq 0.3\text{--}0.5 \text{ m s}^{-2}$.

[5] It is well known that localized neutral winds and secondary GWs are generated from horizontal body forces in nonviscous fluids [*Zhu and Holton*, 1987; *Fritts and Luo*, 1992; *Luo and Fritts*, 1993; *Vadas and Fritts*, 2001 (hereinafter VF2001); *Vadas et al.*, 2003 (hereinafter V2003)]. Studies of 2-D and 3-D impulsive or step function horizontal body forcings [*Dickinson*, 1969; *Blumen*, 1972; *Walterscheid and Boucher*, 1984; *Zhu and Holton*, 1987; *Fritts and Luo*, 1992; *Luo and Fritts*, 1993; *Bühler et al.*, 1999] and 3-D smoothly varying in time horizontal body forces (V2003) have been performed. Although viscosity was not included in V2003, VF2006 suggested that the neutral response to a thermospheric body force would be the excitation of large-scale GWs and the creation of a large neutral wind perturbation at the location of the body force.

[6] Because GWs with $c_H > 250\text{--}300 \text{ m/s}$ cannot propagate in the lower atmosphere, it has traditionally been assumed that large-scale, fast LSTIDs could only arise from Joule heating in the auroral zone [e.g., *Hocke and Schlegel*, 1996]. However, many studies have shown that large-scale GWs (with unknown sources) are ubiquitous in the thermosphere during geomagnetically quiet conditions [*Hedin and Mayr*, 1987; *Mayr et al.*, 1990; *Forbes et al.*, 1995; *Bruinsma and Forbes*, 2008]. This paper resolves this mystery by presenting a robust mechanism for the excitation of large-scale GWs in the thermosphere that is independent of geomagnetic activity. The driver for this mechanism is the dissipation of upward propagating small- and medium-scale GWs at altitudes of $z \sim 120\text{--}250 \text{ km}$.

[7] The purpose of this paper is to determine the response of the thermosphere and ionosphere to the dissipation of GWs excited from a deep convective plume. In section 2, we review the convective plume, ray trace, and TIME-GCM models. Section 3 provides a description of the estimated convective plume parameters. In section 4, we describe the propagation and dissipation of the GWs excited from a deep convective plume in Brazil. Section 5 describes the neutral and plasma responses to the thermospheric body force created from the dissipation of these GWs. In section 6, we describe the daily variability of the thermospheric body forces. A discussion of published data which supports this

mechanism is provided in section 7. Our conclusions are provided in section 8.

2. Methodology

2.1. Convective Plume Model

[8] Many nonlinear models of GW excitation from convection have been developed [*Piani et al.*, 2000; *Horinouchi et al.*, 2002; *Lane et al.*, 2001, 2003]. Linear models which calculate the generation of GWs from convection either consider a localized heating in the lower stratosphere [*Alexander et al.*, 1995; *Walterscheid et al.*, 2001; *Beres*, 2004] or an upward acceleration of air [*Stull*, 1976; *Vadas and Fritts*, 2004; VF2009]. We consider the latter excitation mechanism here, which models the upward acceleration of air in the vertical momentum equation as a “vertical body force.” Physically, high-frequency GWs are excited when a convective plume overshoots the tropopause by up to 1–3 km, rapidly displacing the stratospheric air from equilibrium.

[9] The convective plume model we use here models a single occurrence of convective overshoot for the envelope of a convective plume with a diameter of $\mathcal{D} \sim 5\text{--}20 \text{ km}$. The excited high-frequency GWs are described by the Boussinesq dispersion relation:

$$\omega_r^2 \simeq \frac{k_H^2 N^2}{m^2 + k_H^2}, \quad (1)$$

where ω_r is the wave’s intrinsic frequency, (k, l, m) is the wave number vector, $k_H^2 = k^2 + l^2$, and N is the buoyancy frequency. The zonal, meridional, and vertical wavelengths are $\lambda_x = 2\pi/k$, $\lambda_y = 2\pi/l$, and $\lambda_z = 2\pi/m$, respectively. Additionally, the horizontal wavelength is $\lambda_H = 2\pi/k_H$. The approximate amplitudes and scales of the excited model GWs have been verified with observations of concentric rings in the OH layer from observed deep convective plumes during nearly windless conditions [*Vadas et al.*, 2009b]. This model gives good agreement for GWs with $\lambda_H \sim 20\text{--}100 \text{ km}$ and $\tau_r = 5\text{--}15 \text{ min}$. We refer the reader to VF2009 and *Vadas et al.* [2009b] for additional convective plume model details.

2.2. Ray Trace Model

[10] Ray tracing has been used for decades for geophysical problems of interest [e.g., *Jones*, 1969; *Marks and Eckermann*, 1995; *Cowling et al.*, 1971; *Waldock and Jones*, 1984, 1987; *Hung and Kuo*, 1978; *Hung and Smith*, 1978; *Lighthill*, 1978; *Gerrard et al.*, 2004; *Hecht et al.*, 2004]. Our ray trace model allows the wind, density, and other background parameters to change slowly with altitude and horizontal location.

[11] The GW dispersion relation we use here includes one of the most important damping mechanisms in the thermosphere for high-frequency GWs with large λ_z : kinematic viscosity and thermal diffusivity. It is nonhydrostatic and compressible, but excludes acoustic waves. The effects of wave breaking and saturation are not included here (see *Yigit et al.* [2008, 2009] for a parameterization which includes these effects). Therefore, the thermospheric body forces are due entirely to kinematic viscosity and thermal diffusivity,

not wave breaking. This dissipative, anelastic GW dispersion relation is (VF2005, equation (26))

$$m^2 = \frac{k_H^2 N^2}{\omega_{lr}^2 (1 + \delta_+ + \delta^2 / \text{Pr})} \cdot \left[1 + \frac{\nu^2}{4\omega_{lr}^2} \left(\mathbf{k}^2 - \frac{1}{4H^2} \right)^2 \frac{(1 - \text{Pr}^{-1})^2}{(1 + \delta_+ / 2)^2} \right]^{-1} - k_H^2 - \frac{1}{4H^2}, \quad (2)$$

where $\mathbf{k}^2 = k_H^2 + m^2$, $\nu = \mu/\bar{\rho}$ is the kinematic viscosity, μ is the viscosity coefficient, $\text{Pr} = 0.7$ is the Prandtl number, $\bar{\rho}$ is the background density, $H = -\bar{\rho}/(d\bar{\rho}/dz)$ is the density scale height, $\delta = \nu m/H\omega_{lr}$, and $\delta_+ = \delta(1 + \text{Pr}^{-1})$. Additionally, the background pressure is related to the density and temperature \bar{T} through the ideal gas law: $\bar{p} = R\bar{\rho}\bar{T}$. This dissipative dispersion relation yields the usual high-frequency GW anelastic dispersion relation when dissipation is negligible, obtained by setting $\nu = \delta = \delta_+ = 0$ in equation (2):

$$\omega_{lr}^2 \simeq \frac{k_H^2 N^2}{m^2 + k_H^2 + 1/4H^2} \quad (3)$$

[Gossard and Hooke, 1975]. Equation (3) differs from equation (1) in that the Boussinesq approximation assumes that $\lambda_z \ll 4\pi H$.

[12] Above the turbopause (at $z \sim 110$ km), a high-frequency, small-amplitude GW is damped primarily by kinematic viscosity and thermal diffusivity. It dissipates rapidly above the altitude where

$$c_{g,z}/2\omega_{li} \sim H \quad (4)$$

(VF2005, equation (54)), where $c_{g,z}$ is the vertical group velocity,

$$c_{g,z} = \partial\omega_{lr}/\partial m, \quad (5)$$

and ω_{li} is the dissipative decay rate (VF2005):

$$\omega_{li} = -\frac{\nu}{2} \left(\mathbf{k}^2 - \frac{1}{4H^2} \right) \frac{[1 + (1 + 2\delta)/\text{Pr}]}{(1 + \delta_+/2)}. \quad (6)$$

For a GW with $\mathbf{k}^2 \simeq m^2 \gg 1/4H^2$ which is weakly dissipating ($|\delta| \ll 1$), equation (6) becomes

$$\omega_{li} \sim -\nu(1 + \text{Pr}^{-1})\mathbf{k}^2/2 \sim -\nu(1 + \text{Pr}^{-1})m^2/2. \quad (7)$$

Using the same approximations, equation (5) becomes

$$c_{g,z} \simeq -\omega_{lr}/m. \quad (8)$$

Therefore, using equation (4), a GW dissipates rapidly above the altitude given by

$$\frac{\lambda_z^3 \omega_{lr}}{8\pi^3 H (1 + \text{Pr}^{-1})} \sim \nu. \quad (9)$$

Since ν increases approximately exponentially with altitude, equation (9) shows that GWs with the largest λ_z and ω_{lr} survive to the highest altitudes before dissipating, although

the dependence is stronger for λ_z than for ω_{lr} [Vadas, 2007 (hereinafter V2007), and references therein; Miyoshi and Fujiwara, 2008]. If, however, a GW reaches an altitude where $\omega_{lr} \simeq N$, then it will reflect downward at this altitude, neglecting wave tunneling.

[13] For each convective plume, ~ 2 million GWs are inserted into the ray trace model at the same location and time. Because ν is negligible in the lower atmosphere, we recalculate ω_{lr} using equation (3). The background zonal and meridional winds are U and V , respectively. U , V , and \bar{T} depend on (x, y, z, t) . We do not allow the ground-based frequency of a GW, ω_r , to vary in time; this follows the assumption that U , V , and \bar{T} vary slowly in time. Other formulations take ω_r changing in time into account [e.g., Jones, 1969].

[14] The average momentum flux amplitudes, $u w^*$ and $v w^*$, and average wave numbers (weighted by the horizontal momentum flux perturbations) are saved in 4D arrays with bin sizes Δx , Δy , Δz , and Δt in x , y , z and t , respectively. Here, we set $\Delta x = \Delta y$. Additionally, GW phases were recently added to the ray trace model, thereby allowing for the reconstruction of the GW field. Note that the reconstructed ray trace solutions approximate well the exact Boussinesq solutions in a windless, isothermal environment for wave frequencies and scales where H can be neglected (VF2009). We refer the reader to V2007, VF2009, and Vadas *et al.* [2009b] for additional ray trace model details.

2.3. TIME-GCM

[15] The NCAR Thermosphere-Ionosphere-Mesosphere-Electrodynamics General Circulation Model (TIME-GCM) simulates the circulation, temperature and compositional structures of the upper atmosphere (30–500 km) and the ionosphere, and it includes the dynamical, chemical, and electrodynamical processes in that atmospheric region. Details of the model are given by Roble and Ridley [1994], Roble [1995, 2000], and references therein. Currently TIME-GCM can be run at two resolutions: regular resolution (2 grids/scale height and $5^\circ \times 5^\circ$) and high resolution (4 grids/scale height and $2.5^\circ \times 2.5^\circ$). We use the high-resolution TIME-GCM for the thermospheric body force simulation shown here, with forcing at the lower boundary specified by the European Centre for Medium-range Weather Forecast (ECMWF) reanalysis data.

3. Thermospheric Body Forces From a Deep Convective Plume

[16] GWs transport momentum. Thus, when they dissipate in the thermosphere, they create a thermospheric horizontal body force [Hines, 1972]. The direction of the thermospheric body force created from GWs excited from deep convection is simple to determine if the background wind direction is assumed constant with altitude; if the background winds are westward (Wward), then the thermospheric body force is eastward (Eward) (VF2006). However, the background winds change direction with altitude in the thermosphere because of diurnal and semidiurnal tides and other waves. Here, we calculate the body force created from a deep convective plume on 1 October using realistic wind and temperature profiles.

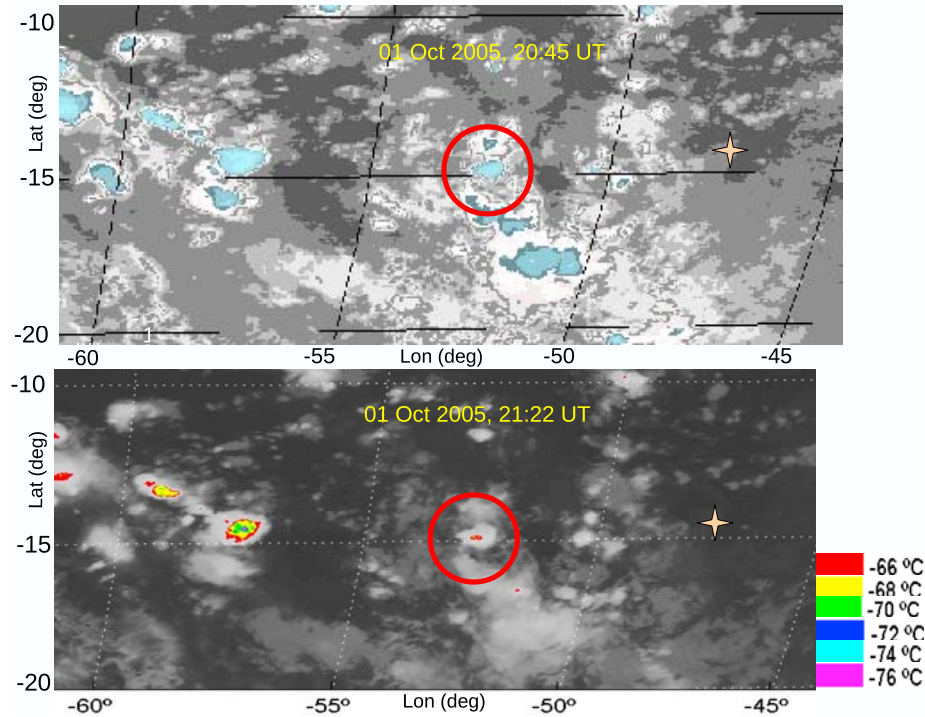


Figure 1. Infrared satellite images showing convection over Brazil on 1 October (top) at 2045 UT and (bottom) at 2122 UT. The convective plume we model here is located at the center of the red circles. The location of the OH imager near Brasilia is marked as four-pointed peach stars.

3.1. Convective Plume Parameters

[17] We choose an isolated, deep convective plume that occurred on 1 October 2005, at 2122 UT, 52.5°W and 15.0°S, during the SpreadFEx campaign in Brazil. A reverse ray trace study identified this plume as exciting a GW with $\lambda_H = 71.4$ km, $c_H = 58$ m/s, and $\tau_r = 21$ min that was observed at 2306 UT in the OH airglow layer near Brasilia [Vadas *et al.*, 2009a]. This analysis took into account wind uncertainties and ground reflection.

[18] Figure 1 (top) shows a satellite image on 1 October 2005 at 2045 UT. This image shows the brightness temperatures (equivalent blackbody temperature) in the infrared (IR) band, which is a surrogate for (but does not equal) the actual temperature [see, e.g., Menzel and Purdom, 1994, and references within]. Light blue shading indicates regions where colder cloud material is located near the tropopause. Localized dark blue shading denotes regions with the coldest brightness temperatures, indicative of regions of active convection. Since the local time (LT) is the universal time (UT) minus 3 h, 2100 UT corresponds to 1800 LT, which is about 1–1.5 h before sunset. The convective plume we model here is within the red circle. Figure 1 (bottom) shows a GOES 12 satellite image on 1 October 2005 at 2122 UT. This image has been color coded for temperatures from -66°C to -76°C . Localized cold temperatures on the anvils imply convective overshoot, because a parcel of air which moves adiabatically through the tropopause and into the stratosphere has a colder temperature than the surrounding air. Using these images, we estimate a full-width horizontal diameter for this convective plume of $D_H = 15$ km. Additionally, the maximum possible depth of a convective plume is the depth of the

troposphere plus 1–3 km for convective overshoot. We choose an overshoot altitude of 1 km, and a full depth of $D_z = 10$ km to account for the fact that the GWs are only excited when the air parcels push the stratospheric air upward just below and above the tropopause. To account for the fact that only some of the air is moving upward rapidly at z_{trop} , we choose a “filling factor” of $\epsilon = 0.75$, as this value agrees well with OH observations [Vadas *et al.*, 2009b]. We choose a convective overshoot time of $t = 2120$ UT, as identified by Vadas *et al.* [2009a]. Finally, we determine an average tropopause altitude of $z_{\text{trop}} = 13.6$ km from 3 nearby balloon soundings. The top of the body force is thus at $z = 14.6$ km, and the center of the body force is at $z = 9.6$ km.

[19] Because each excited GW’s amplitude is linearly proportional to the updraft velocity of the convective plume, w_{pt} , the resulting thermospheric body force is proportional to w_{pt}^2 . Therefore, it is important that we estimate the convective plume updraft velocity as accurately as possible. We do this via the Convective Available Potential Energy (CAPE) [Bluestein, 1993]. Figure 2 shows a map of the CAPE on 1 October at 1800 UT, 3 h before the images in Figure 1. At this time, the CAPE in the vicinity of the convective plume is ~ 600 – 800 J/kg. The CAPE is the maximum kinetic energy per mass available to a parcel of air. Therefore, the maximum upward velocity for a convective plume in this region is

$$w \sim \sqrt{2\text{CAPE}}. \quad (10)$$

Although equation (10) is the upper limit for the maximum updraft velocity of a convective plume in this area, a

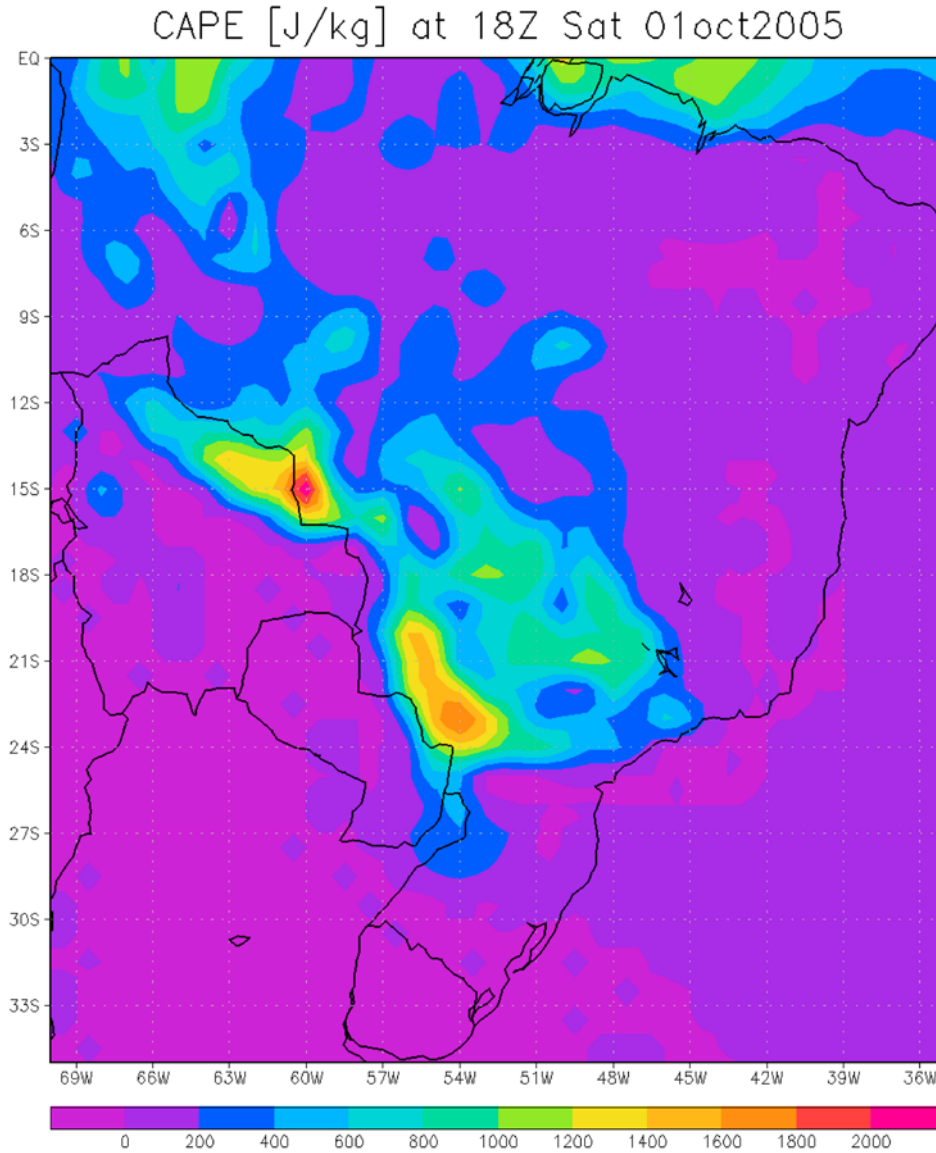


Figure 2. A map of the CAPE on 1 October at 1800 UT.

balloon experiment showed that the velocity of the updraft equaled equation (10) for one storm [Bluestein *et al.*, 1988]. Therefore, we set $w_{p1} \sim \sqrt{2\text{CAPE}} \sim 35\text{--}40$ m/s. Here, we choose a conservative updraft velocity of $w_{p1} = 35$ m s⁻¹. This is identical to that utilized in a study of the excitation and propagation of concentric rings excited by a deep convective plume in Colorado [Vadas *et al.*, 2009b].

[20] Because the amplitudes are increasingly small for GWs with $\omega_{Ir} \ll 2\pi/s_t$ (VF2001), we choose a total plume duration of $s_t = 10$ min here in order to allow for the excitation of GWs with periods of $\sim 5\text{--}10$ min and with reasonably large wave amplitudes [Vadas *et al.*, 2009b]. This duration is reasonable, because the movement of air which excites the GWs (the upwelling just below the tropopause, the overshoot, and the collapse back down to the tropopause) lasts for approximately 5–15 min in convective simulations.

[21] Figure 3 shows the primary GW spectrum excited by this plume. The amplitudes correspond to the GW horizon-

tal velocity amplitudes at $z = 87$ km if the intervening winds are zero. We also overlay the intrinsic horizontal phase velocity, $c_{IH} = \omega_{Ir}/k_H$, and the vertical group velocity, c_{gz} . The peak of this spectrum occurs at $\lambda_H \sim 50$ km and $\lambda_z \sim 30$ km. There is a smaller peak at $\lambda_H \sim 25$ km and $\lambda_z \sim 12$ km because of partial destructive interference of the waves at $\lambda_z \sim 15\text{--}20$ km, since the vertical distance between the force and its image is ~ 19 km. We also overlay intrinsic GW periods of $\tau_{Ir} = 2\pi/\omega_{Ir} = 10$ and 30 min. These are the intrinsic wave periods of most importance in the thermosphere from lower atmospheric GW sources [V2007; FV2008]. We see that the bulk of the GW spectrum with $\lambda_H > 100$ km and $c_{IH} > 100$ m s⁻¹ lie within these lines.

[22] It was found by Vadas *et al.* [2009a] that the GW observed in the OH airglow layer with $\lambda_H = 71.4$ km had $\lambda_z \sim 24$ km at the tropopause, and an estimated horizontal wind amplitude of $u_H \sim 10$ m s⁻¹ in the OH layer. Using Figure 3, a GW excited from this modeled convective plume with $\lambda_H = 71.4$ km and $\lambda_z \sim 24$ km has an amplitude of $u_H \sim$

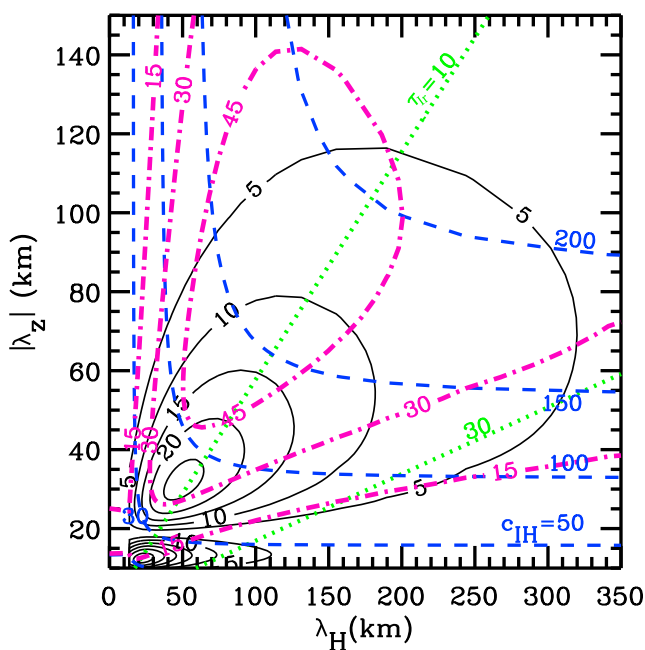


Figure 3. Convective GW spectrum. Shown are the GW horizontal velocity amplitudes at $z = 87$ km in intervals of 5 m s^{-1} if the winds are zero (black lines). These are the maximum amplitudes at this altitude. Pink dash-dot lines indicate c_{gz} in 15 m s^{-1} intervals. Blue dash lines indicate the intrinsic horizontal phase speed c_{HH} in 50 m s^{-1} intervals. The green dotted lines show $\tau_{Tr} = 10$ and 30 min.

$13\text{--}14 \text{ m s}^{-1}$ at $z = 87$ km. This agrees well with the estimated amplitude of the observed GW.

3.2. Neutral Winds and Temperatures

[23] The horizontal wind and temperature model we employ here was discussed in detail by *Vadas et al.*

[2009a]. Figure 4 shows the zonal and meridional winds at $z = 120, 200,$ and 300 km as a function of time on 1–2 October 2005. At $z = 200$ and 300 km, the winds are dominated by the diurnal tide. At $z = 120$ km, although the meridional wind is dominated by the diurnal tide, the zonal wind contains diurnal and semidiurnal tides, and other wave components. This is important, as the direction of the thermospheric body force is determined by the winds at $z \approx 120$ km (see section 4.2). Note that the horizontal wind is approximately zero at 2000–2130 UT.

[24] Figure 5 shows the winds and temperatures at 2230 UT, approximately 70 min after convective overshoot. We see that the zonal and meridional winds are weak, and change direction frequently with altitude.

4. Response of the Mesosphere and Thermosphere to a Convective Plume

4.1. Neutral Density Perturbations of Freely Propagating GWs

[25] We locate all GWs excited from the modeled convective plume (see Figure 3) at $52.5^\circ\text{W}, 15^\circ\text{S}$, and $z = z_{\text{trop}} = 13.6$ km at $t = 2120$ UT. We then ray trace these GWs into the lower atmosphere and thermosphere. For $z = 40\text{--}120$ km, we save the high-resolution ray trace results in bin sizes of $\Delta x = \Delta y = 12$ km. For $z = 140\text{--}220$ km, we save the results in bin sizes of $\Delta x = \Delta y = 20$ km. The vertical and temporal bin sizes are $\Delta z = 4$ km and $\Delta t = 4$ min, respectively, for both.

[26] Figure 6 shows horizontal slices of the reconstructed GW neutral density perturbations, $\rho'/\bar{\rho}$, in intervals of 20 km from $z = 60$ to 220 km. These slices are shown every 10 min from 2136 to 2255 UT. The maximum wave amplitude for each image varies, as listed in the caption. The times for each image were chosen to show the GWs which create the body force at its maximum location and time (see section 4.2). We see several important features. First, the GWs have horizontal

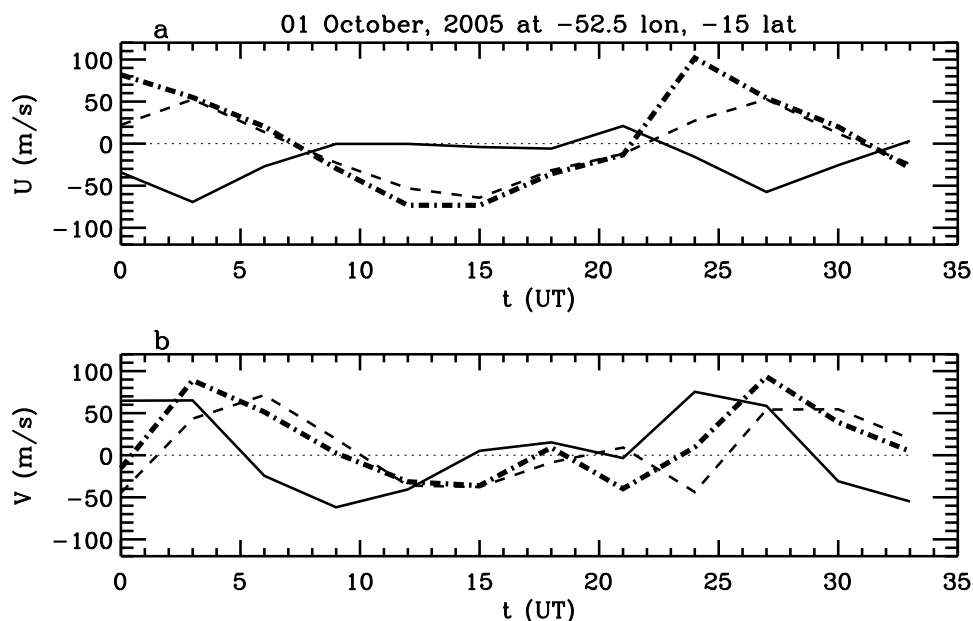


Figure 4. The (a) zonal and (b) meridional winds on 1–2 October 2005 at the plume location, 52.5°W and 15.0°S . Solid, dash, and dash-dot lines show the winds at $z = 120, 200,$ and 300 km, respectively.

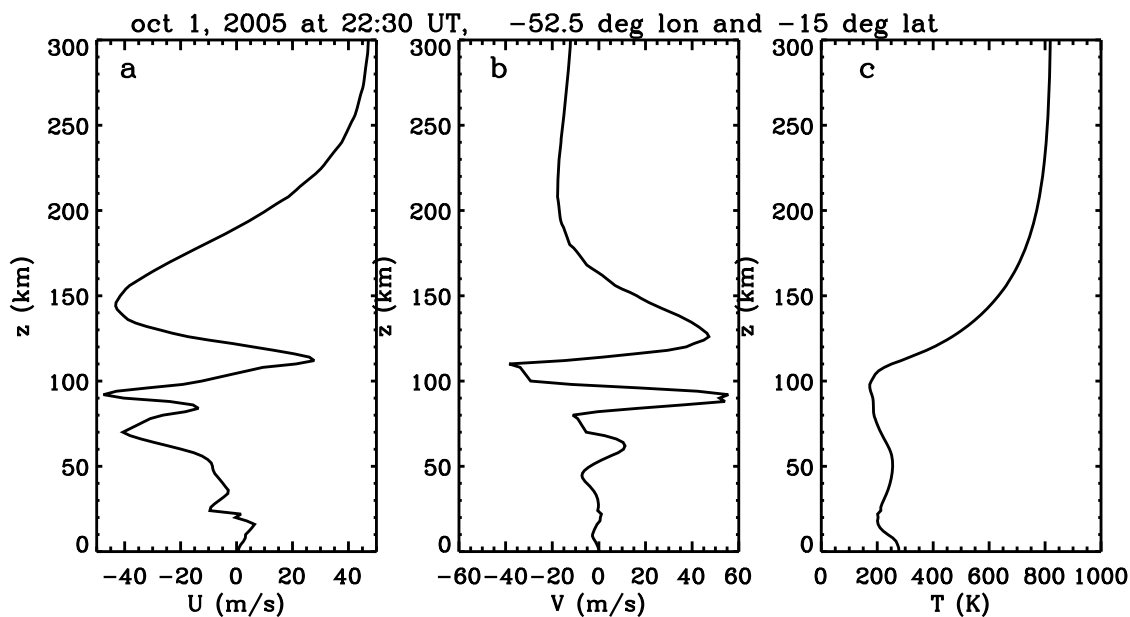


Figure 5. (a) Zonal wind, (b) meridional wind, and (c) temperature profiles at the plume location, 52.5°W and 15°S, on 1 October 2005 at 2230 UT.

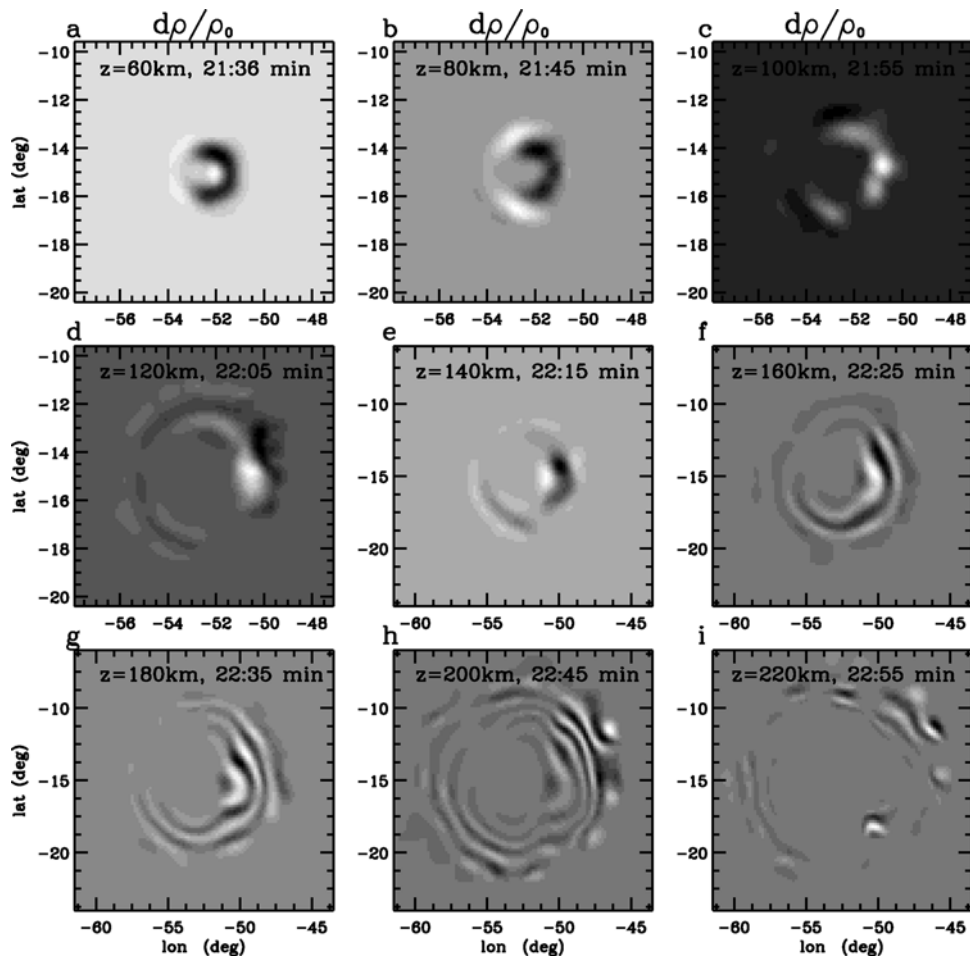


Figure 6. Horizontal slices of $\rho'/\bar{\rho}$ at $z = 60, 80, 100, 120, 140, 160, 180, 200,$ and 220 km at 2136, 2145, 2155, 2205, 2215, 2225, 2235, 2245, and 2255 UT, respectively, as labeled. Maximum positive values are white, and maximum negative values are black. The maximum values of $|\rho'/\bar{\rho}|$ are (a–c) 0.1, 0.3, and 2%; (d–f) 5, 8, and 11%; and (g–i) 11, 5, and 2%. Note that the longitude/latitude scales vary.

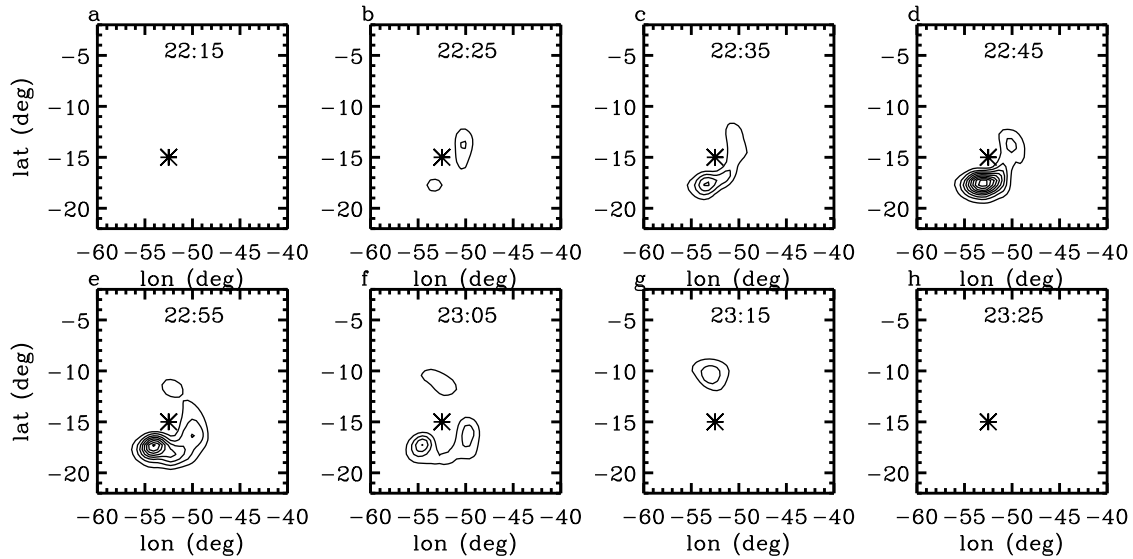


Figure 7. Horizontal cross sections of the thermospheric body force every 10 min from 2215 to 2325 UT at $z = 180$ km. The contours are shown in 10% increments of 1.4 m s^{-2} . Asterisks show the location of the convective plume.

wavelengths of $\lambda_H \sim 60\text{--}100$ km. Second, although the GWs appear as $\sim 270^\circ$ concentric rings at $z = 60\text{--}80$ km, they appear instead as partial “arcs” for $z \geq 100$ km because of increasing thermospheric winds. At $z \sim 200$ km, the “arcs” only appear NE of the convective plume, are relatively linear, and represent freely propagating GWs. The wave fronts S and SE of the plume, however, have smaller amplitudes because of wave dissipation. Third, localized regions have $|\rho'/\bar{\rho}|$ as large as 11% at $z \sim 160\text{--}180$ km.

4.2. Thermospheric Body Force Created From GW Dissipation

[27] We now determine the body force accompanying wave dissipation in the thermosphere. We define the vector thermospheric horizontal body force in the horizontal direction as $\mathbf{F}_b(x, y, z, t)$. The zonal and meridional components of the body force are calculated via

$$\begin{aligned} \mathbf{F}_b \cdot \hat{\mathbf{i}} &= -\frac{1}{\bar{\rho}} \frac{\partial(\overline{\rho u w^*})}{\partial z} \\ \mathbf{F}_b \cdot \hat{\mathbf{j}} &= -\frac{1}{\bar{\rho}} \frac{\partial(\overline{\rho v w^*})}{\partial z}, \end{aligned} \quad (11)$$

respectively [Andrews *et al.*, 1987]. Here, the overlines denote averages over 1–2 wave periods and wavelengths, and $\hat{\mathbf{i}}$ and $\hat{\mathbf{j}}$ are the unit vectors in the zonal and meridional geographic directions, respectively.

[28] We ray trace the GWs excited from the convective plume into the thermosphere again, and save the results in an array with a much larger vertical range of $z = 100$ to 400 km. In order to average the results sufficiently over a wave period and horizontal wavelength, we save the results in larger bin sizes of $\Delta x = \Delta y = 50$ km, $\Delta z = 4$ km, and $\Delta t = 10$ min. Here, it is not necessary to choose a larger vertical bin because we smooth the GW momentum fluxes horizontally (over 150 km) and vertically (over 12 km) prior to calculating the thermospheric body force. Figure 7 shows a time sequence of

the horizontal slices of the thermospheric body force using equation (11), at its maximum altitude of $z = 180$ km. This body force covers a relatively large horizontal distance in the thermosphere because of the large angle subtended by GWs with differing periods that dissipate to create this body force [Hines, 1967]. This is because the angle a GW makes with respect to the vertical, ψ , depends on its period:

$$\cos \psi \simeq \omega_r / N \quad (12)$$

for the windless, Boussinesq approximation [Kundu, 1990].

[29] Because dissipation strongly depends on λ_z and ω_r (see equation (9)), those GWs propagating against the horizontal wind in the lower thermosphere contribute the most to the thermospheric body force. Because the zonal wind is Nward for $115 < z < 185$ km (see Figure 5), the body force is primarily Sward. However, there are also body force components in the SWward, SEward, Eward, and Nward directions. The peak of this body force is S of the convective plume at 53°W , 18°S , and 2245 UT. It has a maximum amplitude of $\sim 1.3 \text{ m/s}^2$, which is somewhat larger than previous estimates (VF2006). We estimate the full widths parallel and perpendicular to the body force direction to be $L_{x'} \sim 400$ km and $L_{y'} \sim 640$ km, respectively. Figure 8 shows vertical slices of the body force every 10 min at the location of the body force. We see that the maximum of the body force moves upward in time, reaching $z \sim 200$ km at 2255 UT, although with a slightly smaller amplitude of 1.2 m/s^2 . From Figure 8, we estimate the full vertical depth of this body force to be $L_z \sim 85$ km. From Figures 7 and 8, we estimate the total duration of this body force to be $L_t \sim 40$ min.

[30] Figure 9 shows horizontal slices of the average horizontal wavelength, the average vertical wavelength, the average intrinsic wave period, and the average observed wave period at the time and altitude when the momentum fluxes are maximum (2245 UT at $z = 184$ km). Here, the

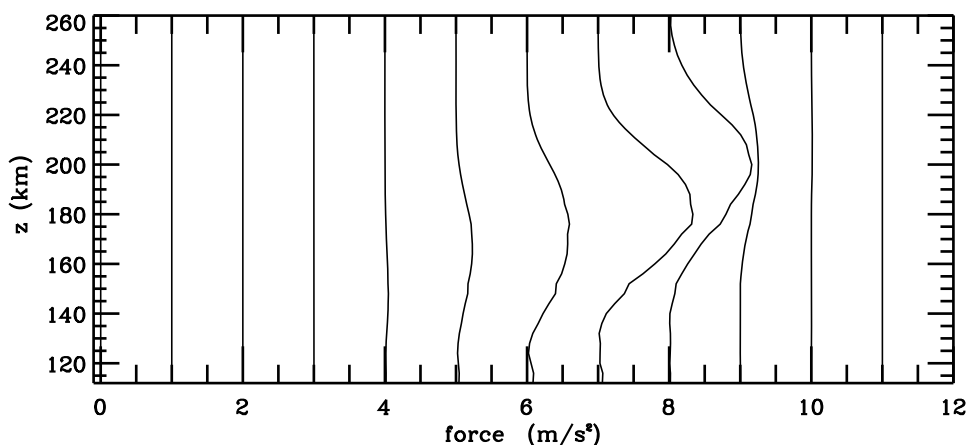


Figure 8. Vertical slices of the body forces shown in Figure 7 at 53.2°W and 17.7°S . Profiles are shown every 10 min from 2135 UT to 2325 UT. Each profile is offset by 1.0 m s^{-2} .

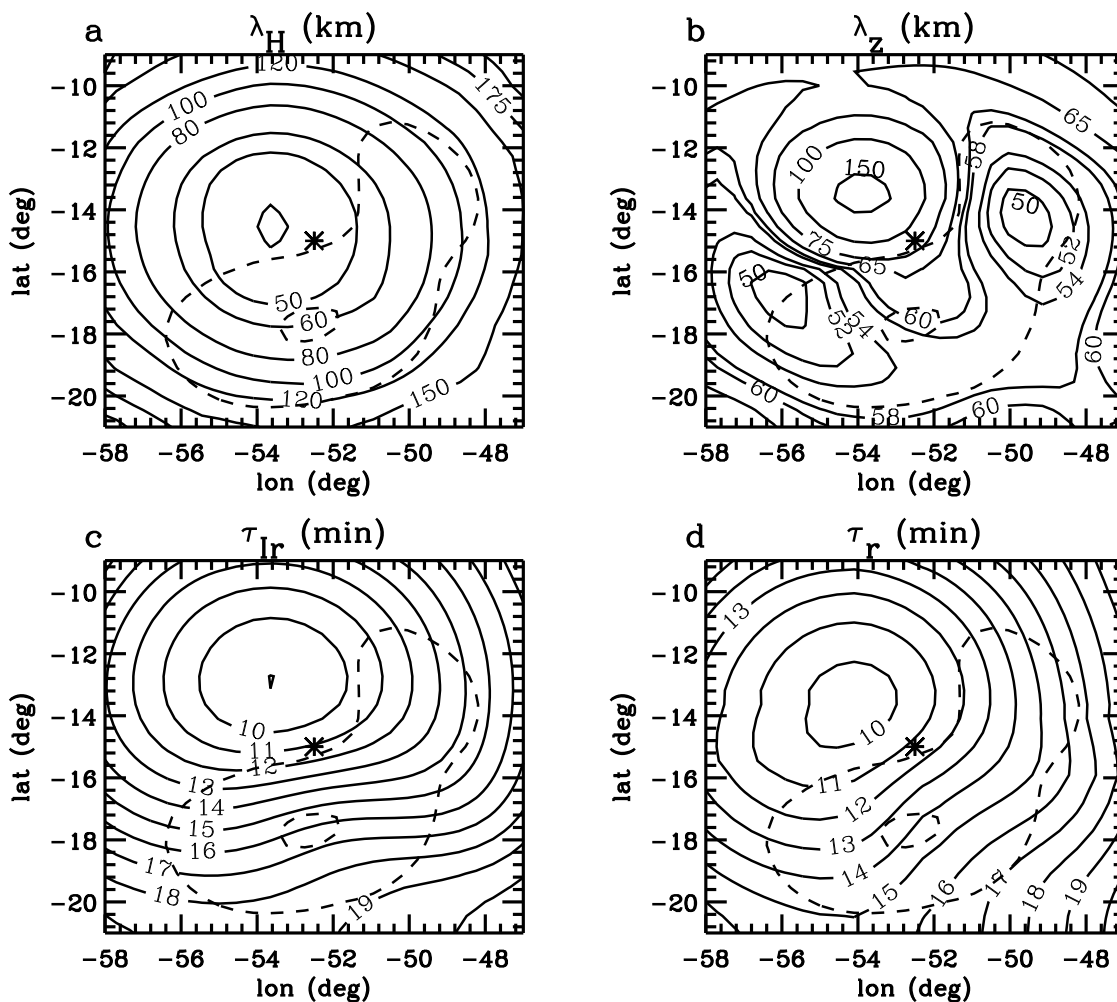


Figure 9. Horizontal slices showing the contours (solid lines) of the averaged (a) horizontal wavelength in kilometers, (b) vertical wavelength in kilometers, (c) intrinsic wave period in minutes, and (d) observed wave period in minutes. Contour lines are unequally spaced, as labeled. These slices are shown at the time and altitude where the vertical flux of horizontal momentum fluxes are maximum: 2245 UT and $z = 184 \text{ km}$. The 10% and 90% contours for the momentum fluxes are also shown as dashed lines. The asterisks show the location of the convective plume.

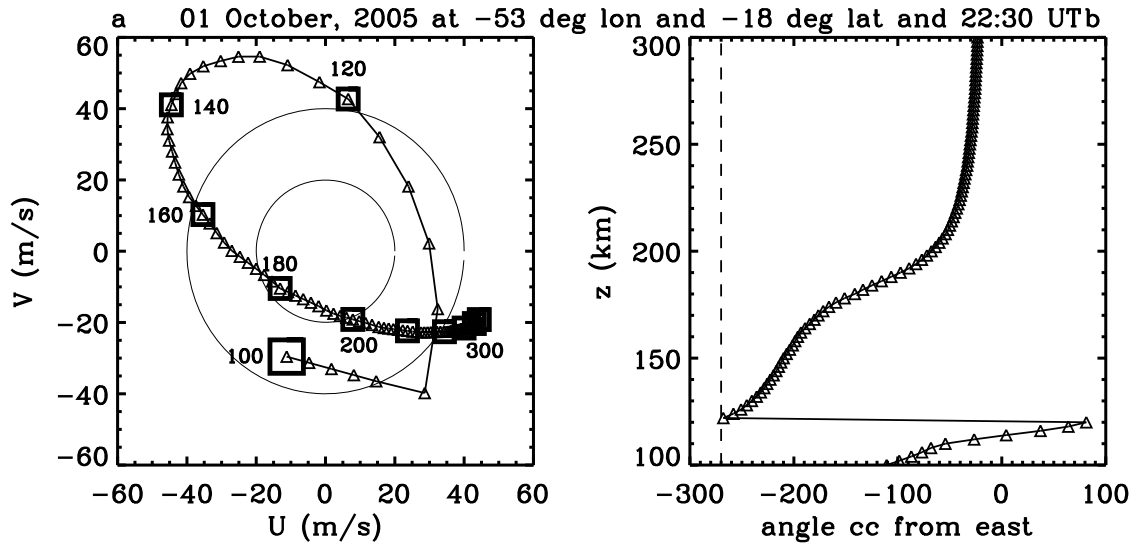


Figure 10. (a) Hodograph of the background horizontal wind from $z = 100$ to 300 km at 53°W and 18°S in Brazil at 2230 UT. The zonal and meridional wind amplitudes are plotted along the x and y axes, respectively. Triangles are every 2 km, the large square denotes the wind at $z = 100$ km, and medium-sized squares indicate the winds every 20 km. Labels denote the altitudes every 20 km from $z = 100$ to 200 km and at $z = 300$ km. (b) Angle of the direction of the horizontal background winds shown in Figure 10a (triangles), counterclockwise (cc) from east. The dash line denotes the direction opposite to the direction of the body force (i.e., Nward).

average horizontal wavelength, vertical wavelength, and wave periods are calculated in each (x, y, z, t) bin by weighting each GW's k_H , m , ω_{Ir} , and ω_r values, respectively, by its horizontal momentum flux amplitude $u_H w^*$:

$$\begin{aligned} \overline{k_H}(x, y, z, t) &= \frac{\sum_i (k_H)_i (u_H w^*)_i}{\sum_i (u_H w^*)_i}, & \overline{m}(x, y, z, t) &= \frac{\sum_i m_i (u_H w^*)_i}{\sum_i (u_H w^*)_i}, \\ \overline{\omega_{Ir}}(x, y, z, t) &= \frac{\sum_i (\omega_{Ir})_i (u_H w^*)_i}{\sum_i (u_H w^*)_i}, & \overline{\omega_r}(x, y, z, t) &= \frac{\sum_i (\omega_r)_i (u_H w^*)_i}{\sum_i (u_H w^*)_i}. \end{aligned} \quad (13)$$

Here, the sum in i includes all of the GWs which enter the (x, y, z, t) bin, and $(u_H w^*)_i = \sqrt{(u w^*)_i^2 + (v w^*)_i^2}$. Then, we compute $\overline{\lambda_H} = 2\pi/\overline{k_H}$, $\overline{\lambda_z} = 2\pi/\overline{m}$, $\overline{\tau_{Ir}} = 2\pi/\overline{\omega_{Ir}}$, and $\overline{\tau_r} = 2\pi/\overline{\omega_r}$. The 10% and 90% contours for the horizontal fluxes of vertical momentum (used to calculate the body forces shown in Figures 7 and 8) are also shown. We see that the GWs of most importance to the creation of the body force have small and medium scales of $\lambda_H \sim 40$ – 150 km, $\lambda_z \sim 50$ – 65 km, $\tau_{Ir} \sim 10$ – 20 min, and $\tau_r \sim 10$ – 20 min. Comparing these values with the GW spectrum excited by this convective plume (see Figure 3), we see that the portion of the initial GW spectrum which creates most of the thermospheric body force is small; indeed, there are many excited GWs with larger λ_z that are likely freely propagating at $z \sim 180$ km, and there are many GWs with smaller λ_z that likely dissipate at lower altitudes (V2007). Many of the GWs with larger λ_z , especially those with $\lambda_z > 100$ km and $\lambda_H > 100$ km, can freely propagate up to the F peak (V2007; FV2008). Therefore, while some of the GWs excited from this convective plume dissipate at $z \sim 180$ km, others freely propagate to higher altitudes before dissipating (see Figure 6). Therefore, the total wind at $z \sim 180$ km is the sum of the background wind, the “mean” wind induced from the

body force (see section 5), and the oscillating wind perturbation from the freely propagating GWs.

[31] As is well known, the neutral, horizontal, background wind in the thermosphere rotates with altitude because of tides and planetary waves. A hodograph of the wind from $z = 100$ to 300 km, ~ 15 min prior to the body force maximum, is shown in Figure 10a. We see that the winds rotate counterclockwise with increasing altitude at this southern latitude location. For $z \gtrsim 260$ km, the winds are relatively constant with altitude because of viscous damping. Figure 10b shows the direction of the wind as triangles, and the direction opposite to the thermospheric body force (i.e., Nward) as a dashed line. We define z_{opp} to be the altitude where the background wind direction is opposite to the direction of the body force. We see that the direction of the body force is determined by the direction of the wind at $z_{\text{opp}} \sim 122$ km, or about 2.4 density scale heights below the body force altitude, since $H \sim 24$ km at $z \sim 180$ km. This is an important result, since it shows that the antiwindward filtering for the thermospheric body force occurs in the lower thermosphere, and therefore depends on the accuracy of the wind model in the lower thermosphere. For our assumed wind model, we show how the body force direction varies as a function of LT in section 6.

[32] Near the F peak, the background neutral wind is SEward. Therefore, the thermospheric body force is oriented in nearly the same direction as the neutral winds near the F peak. Again, this occurs because the body force direction is determined by the wind direction in the lower thermosphere, not by the wind direction at the body force altitude.

5. Neutral and Plasma Responses to the Thermospheric Body Force

[33] As we showed in section 4, a horizontal body force is created in the thermosphere when convectively generated

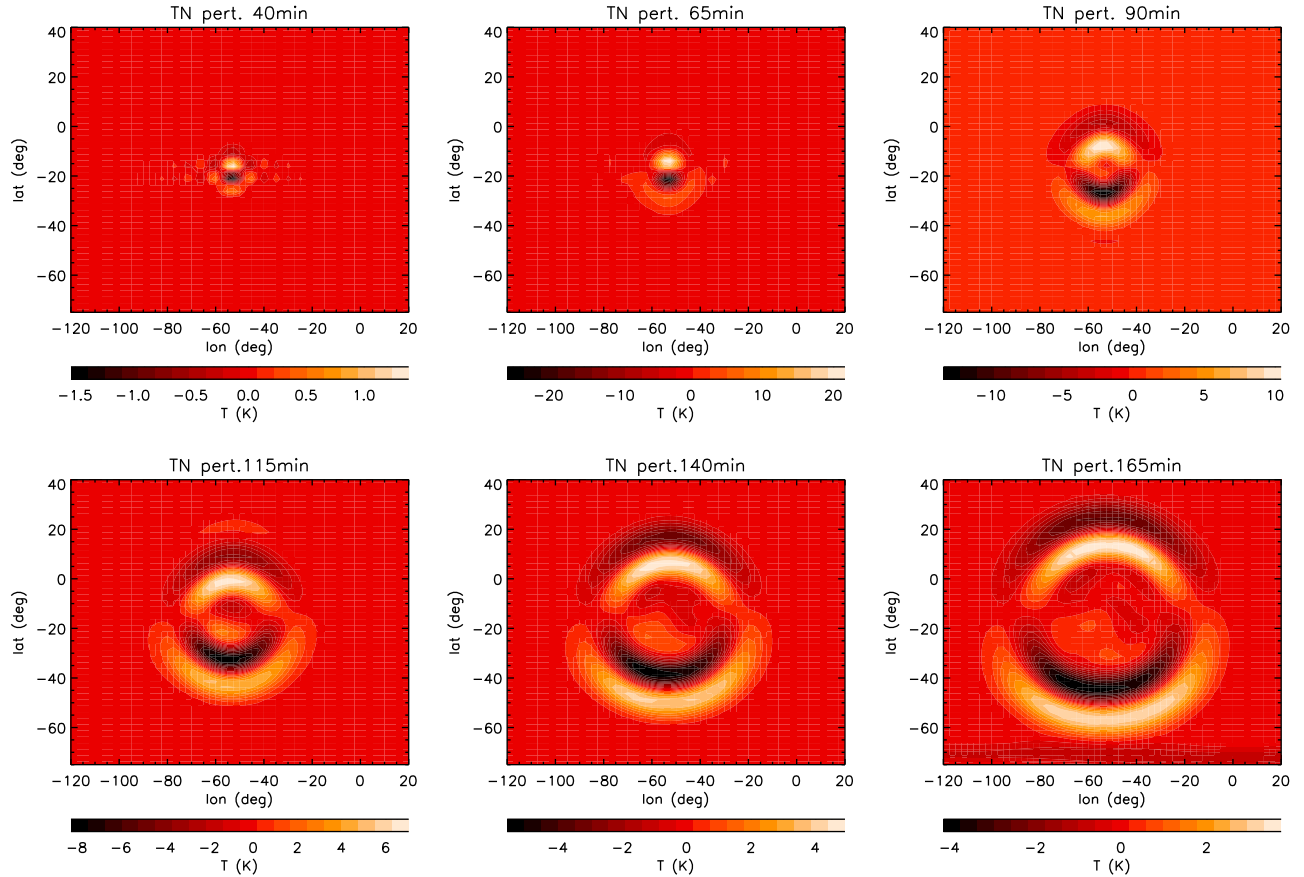


Figure 11. Time series of horizontal slices of T' (in degrees K) at $z = 250$ km induced from the thermospheric body force given by equations (15) and (17). The horizontal slices are shown as a function of longitude and latitude. (top) Shown are T' at $\Delta T =$ (left) 40, (middle) 65, and (right) 90 min. (bottom) Shown are T' at $\Delta T =$ (left) 115, (middle) 140, and (right) 165 min. Note that the color bars are different for each plot. The body force is at $\text{lon}_{\text{max}} = 53.2^\circ\text{W}$ and $\text{lat}_{\text{max}} = 17.7^\circ\text{S}$, near the center of each plot. Additionally, the body force begins at $\Delta T = 24$ min and is maximum at $\Delta T = 45$ min.

GWs dissipate there. Although this body force is complicated spatially and temporally (see Figures 7 and 8), we only wish to study the fundamental changes that this body force affects in the thermosphere here. First, we determine the location where the body force is maximum in geographic coordinates: $x = x_{\text{max}}$, $y = y_{\text{max}}$ and $z = z_{\text{max}}$. Next, we assume that this body force can be represented as a Gaussian in x' , y' and z , with half widths at half max of $\sigma_{x'}$ and $\sigma_{y'}$ in the directions parallel and perpendicular to the direction of the forcing, respectively, and a half depth at half max of σ_z . Here, the transformed coordinates x' and y' are parallel and perpendicular to the body force direction, respectively, and are related to the untransformed coordinates x and y by the standard equations:

$$\begin{aligned} x' &= x \cos \theta + y \sin \theta \\ y' &= -x \sin \theta + y \cos \theta, \end{aligned} \quad (14)$$

where θ is the angle counterclockwise from east in the direction of the body forcing. Finally, we assume that this

body force varies as a cosine in time over its total duration of L_t , with a maximum amplitude of F_0 . Therefore, we parameterize the body force as

$$\begin{aligned} \mathbf{F}_b &= F_0 \exp\left(-\frac{(x' - x_{\text{max}})^2}{2\sigma_{x'}^2} - \frac{(y' - y_{\text{max}})^2}{2\sigma_{y'}^2} - \frac{(z - z_{\text{max}})^2}{2\sigma_z^2}\right) \\ &\quad \cdot f(t) [(\cos \theta)\hat{\mathbf{i}} + (\sin \theta)\hat{\mathbf{j}}], \end{aligned} \quad (15)$$

where

$$f(t) = \begin{cases} \frac{1}{2} \left[1 - \cos\left(\frac{2\pi(t-t_0)}{L_t}\right) \right] = \sin^2\left(\frac{\pi(t-t_0)}{L_t}\right) & \text{for } t_0 \leq t \leq t_0 + L_t \\ 0 & \text{for } t \leq t_0 \text{ and } t \geq t_0 + L_t. \end{cases} \quad (16)$$

Here, t_0 is the initial time that the body force begins, and $t_{\text{max}} = t_0 + L_t/2$ is the time when the body force is maximum.

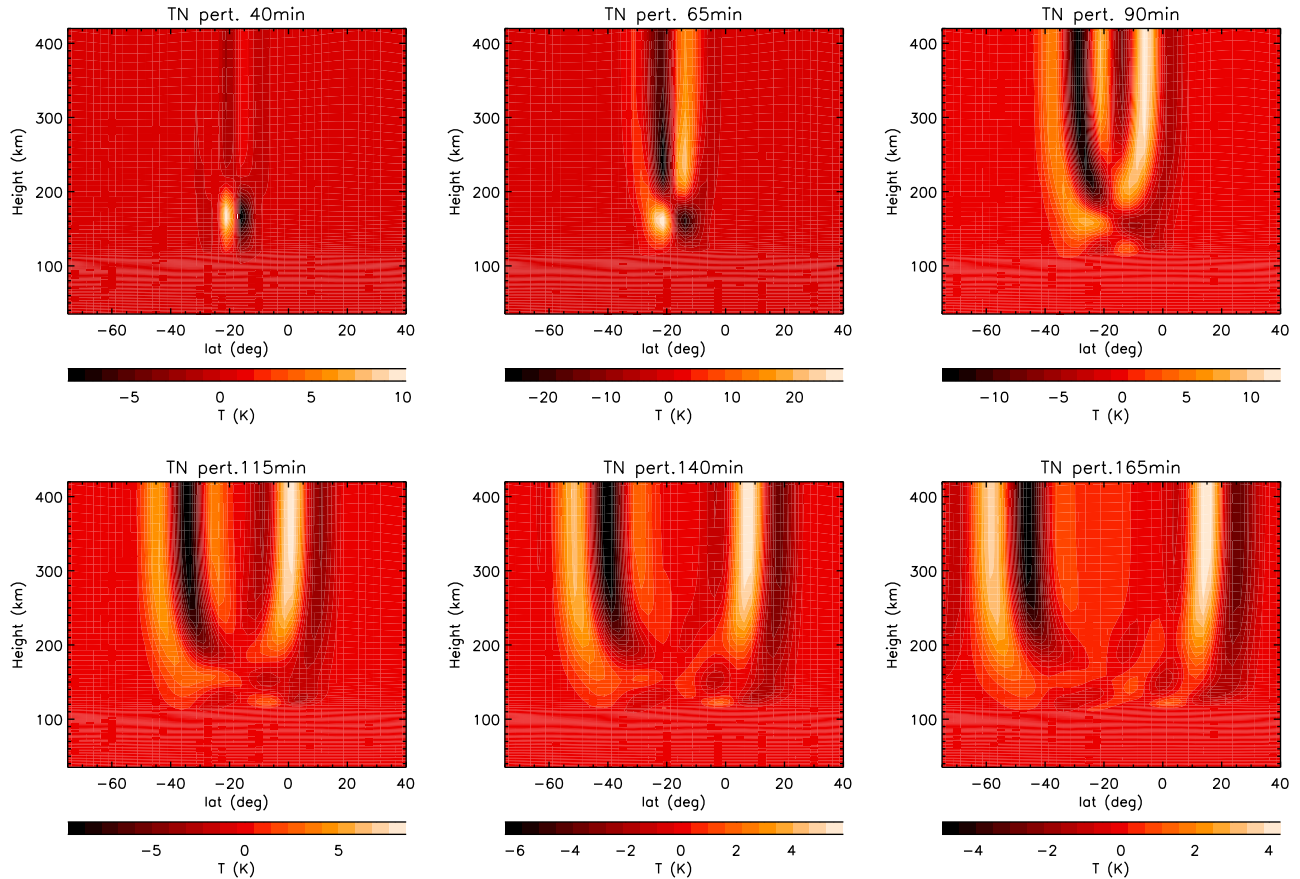


Figure 12. Time series of latitude-vertical slices of T' (in degrees K) at 52.5°W . (top) Shown are T' at $\Delta T =$ (left) 40, (middle) 65, and (right) 90 min. (bottom) Shown are T' at $\Delta T =$ (left) 115, (middle) 140, and (right) 165 min.

Using Figures 7 and 8, the largest-amplitude portion of the thermospheric body force has

$$\begin{aligned}
 F_0 &= 1.33 \text{ m/s}^2, \quad \theta = -90^\circ, L_{x'} = 400 \text{ km}, \\
 L_{y'} &= 640 \text{ km}, \quad L_z = 86 \text{ km}, \quad L_t = 42 \text{ min}, \quad \text{lon}_{\text{max}} = 53.2^\circ\text{W}, \\
 \text{lat}_{\text{max}} &= 17.7^\circ\text{S}, \quad z_{\text{max}} = 180 \text{ km}, \quad t_{\text{max}} = 2245 \text{ UT}, \quad (17)
 \end{aligned}$$

where $L_{x'} = 4.5\sigma_{x'}$, $L_{y'} = 4.5\sigma_{y'}$, and $L_z = 4.5\sigma_z$ are the full widths and depths of the body force, respectively, and lon_{max} and lat_{max} are the longitude and latitude corresponding to x_{max} and y_{max} , respectively. We specify $L_{x'}$ here instead of $\sigma_{x'}$, for example, because the nonviscous secondary GW spectrum peaks at $\lambda_{x'} \sim 2L_{x'}$, $\lambda_z \sim (1-2)L_z$, etc (V2003). Note that the body force begins at $t_0 = t_{\text{max}} - L_t/2 \sim 2224 \text{ UT}$.

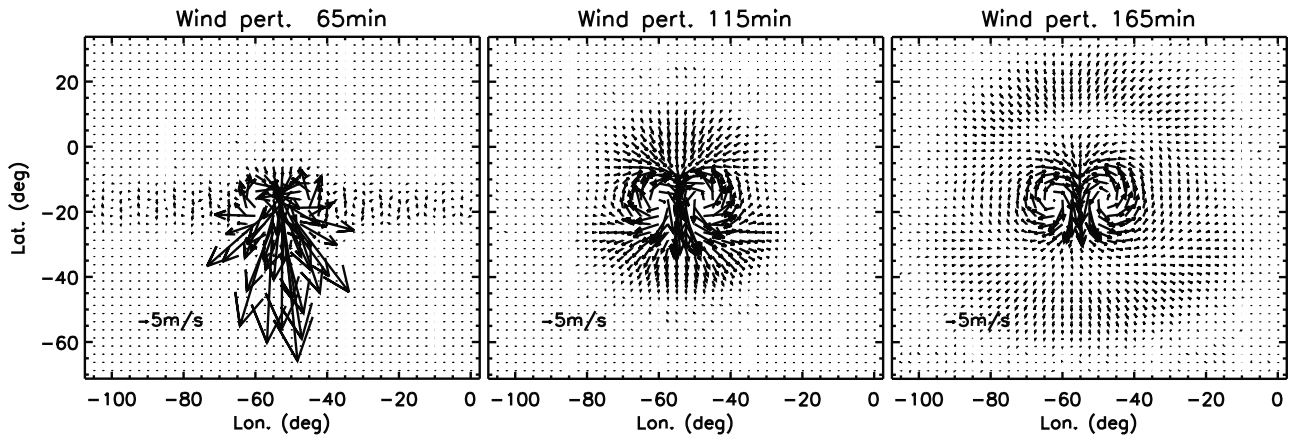


Figure 13. Vector plots of the horizontal wind perturbations (in m s^{-1}) at $z = 183 \text{ km}$ at $\Delta T =$ (left) 65, (middle) 115, and (right) 165 min. The length of each arrow is proportional to the speed, while the direction denotes the direction of fluid flow. A small arrow in the bottom left-hand corner of each plot shows a speed of 5 m s^{-1} .

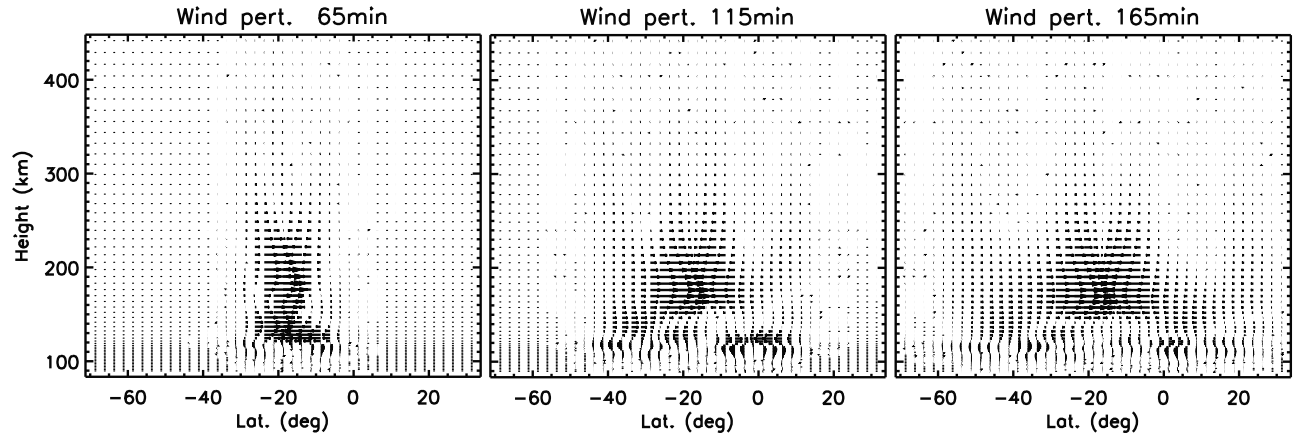


Figure 14. Vector plots of the meridional wind perturbations at 52.5°W . Here, the wind perturbations have been multiplied by \sqrt{p} in order to observe the GW amplitudes at both the lower and higher altitudes. Shown are the results for $\Delta T =$ (left) 65, (middle) 115, and (right) 165 min.

[34] We insert \mathbf{F}_b from equations (15)–(17) into the high-resolution TIME-GCM. We then calculate the difference between this “perturbed” solution and the “unperturbed” high-resolution TIME-GCM solution (i.e., with no thermospheric body force). We now show the local and global responses to this thermospheric body force in Figures 11–18; all plotted quantities are the perturbed minus the unperturbed TIME-GCM solutions. Additionally, all times in Figures 11–18 are shown relative to 2200 UT, i.e.,

$$\Delta T = t - 2200 \text{ UT.} \quad (18)$$

5.1. Neutral Response

5.1.1. Local Response

[35] We first describe the local, neutral response to this body force. We then compare these results with the nonviscous, neutral results.

5.1.1.1. Numerical Results

[36] Figure 11 shows horizontal slices of the temperature perturbations T' as a function of latitude, longitude, and

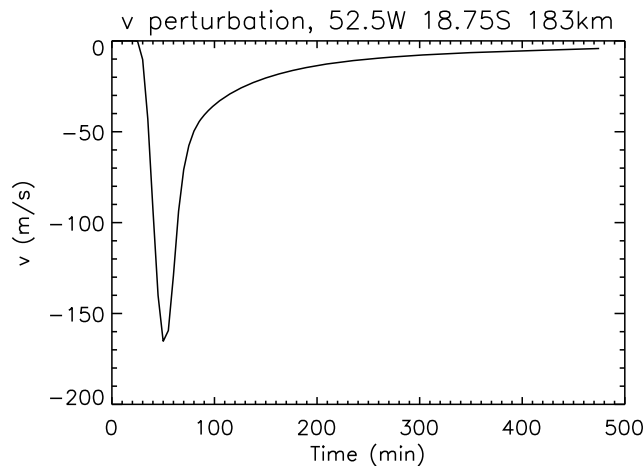


Figure 15. Meridional wind perturbation, v , near the center of the thermospheric body force at $z = 183$ km, 52.5°W and 18.75°S , as a function of time.

time. The slices are ~ 70 km above the body force, at $z = 250$ km. We see that large-scale secondary GWs are excited by the body force. These waves propagate upward and outward from the center of the body force as coherent, concentric, antisymmetric rings. The center of the rings corresponds to the center of the body force. Within an hour of the body force maximum, the secondary GWs propagate Sward and Nward by $\sim 20^\circ$. Therefore, the response spreads out globally, although the wave amplitude decreases with distance away from the center of the body force because the wave occupies a larger area (geometric attenuation). Additionally, the GWs with the largest amplitudes propagate Sward and Nward, in the direction of and against the direction of the body force. However, large-scale secondary GWs also propagate in all other directions except those perpendicular to the body force direction (i.e., Eward and Wward). Note that the secondary GW amplitudes are similar in the Sward and Nward directions.

[37] Figure 12 shows latitude-vertical slices of T' at the same times as in Figure 11, at a longitude close to the center of the body force. Figure 12 shows that the body force

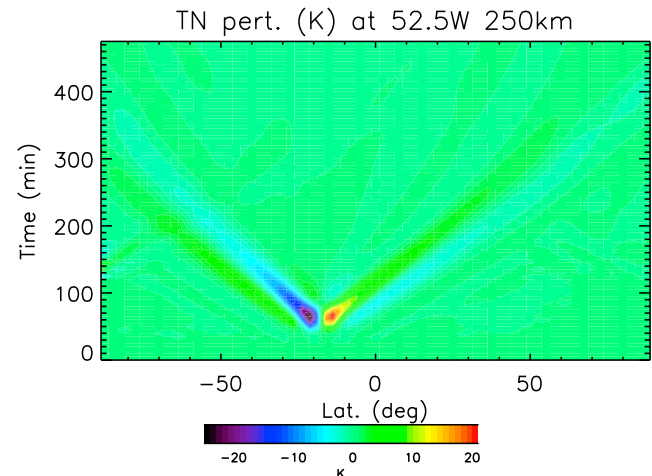


Figure 16. Temperature perturbation (in degrees K) at 52.5°W and $z = 250$ km as a function of latitude and time.

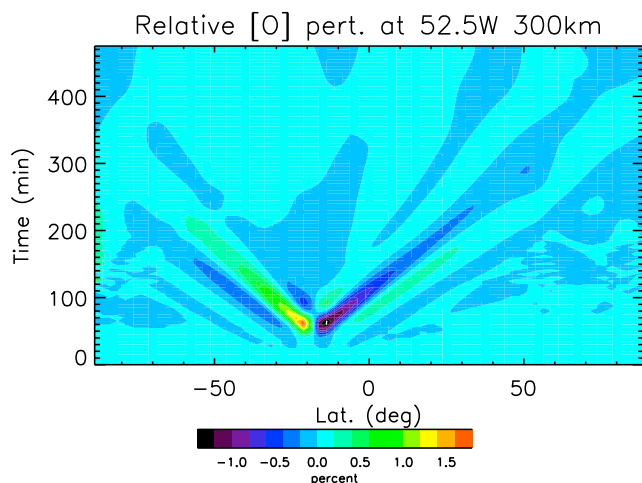


Figure 17. Relative perturbation of [O] (in %) at 52.5°W and $z = 300$ km as a function of latitude and time.

excites both upward and downward propagating GWs. These downward propagating GWs are especially noticeable for $\Delta T \geq 90$ min. We also see that these initially downward propagating GWs reflect upward at $z \sim 120$ km at $\Delta T \sim 90$ – 165 min.

[38] From Figures 11 and 12, we estimate that these large-scale, secondary GWs have horizontal wavelengths of $\lambda_H \sim 2100$ – 2200 km, horizontal ground-based phase speeds of $c_H \sim 480$ – 510 m/s, and observed ground-based periods of $\tau_r \sim 80$ min at $\Delta T \sim 110$ – 170 min. At an earlier time ($\Delta T \sim 90$ min), the horizontal wavelengths are somewhat smaller: $\lambda_H \sim 2000$ km. The amplitude of the secondary GWs is ~ 30 K at $\Delta T = 65$ min, and decreases with time thereafter. At $\Delta T = 165$ min, the amplitude is only ~ 6 K. Because the background temperature is $\bar{T} \sim 825$ K at $z = 250$ (see Figure 5), the maximum temperature perturbation at $z \approx 250$ km is $T'/\bar{T} \sim 3.6\%$. There also appears to be < 1 K asymmetric temperature perturbations directly above the body force at $\Delta T = 140$ – 165 min in Figure 11. These perturbations may be induced from the plasma response to this body force.

[39] In Figure 13, we show a vector plot of the horizontal wind at $z = 183$ km as a function of time. We see that a strong neutral wind is created in the direction of the body force (Sward) at $\Delta T = 65$ min at the location of the body force. By $\Delta T = 115$ min, a horizontal return flow is visible; the Sward moving fluid diverges SEward and SWward at the southern edge of the body force. Both halves then move Nward, and converge on the northern edge of the body force. This creates horizontal neutral wind shears. Note that for all three times, the flow is Sward at the location of the body force. In addition, the horizontal extent of this Sward flow is quite large: ~ 1000 km parallel and perpendicular to the force at $\Delta T = 115$ – 165 min.

[40] In Figure 14, we show the meridional wind perturbations as a function of altitude at the same times as in Figure 13. Here, the wind perturbations have been multiplied by $\sqrt{\bar{p}}$ in order to see the GWs at both the lower and upper altitudes. (For an isothermal fluid (i.e., constant \bar{T}), \bar{p} and $\bar{\rho}$ scale as $\exp(-z/H)$, and the GW amplitudes scale as $1/\sqrt{\bar{p}}$.) Therefore, the values of the vector lengths are meaningless, and so are not shown. However, the relative

lengths of the wind vectors illuminate the GWs and the neutral zonal flow. As in Figure 13, we see that the meridional wind is Sward, with a vertical extent of ~ 80 – 90 km. This creates large vertical wind shears at $z \sim 130$ – 160 km and at $z \sim 210$ – 250 km. The downward propagation of the large-scale secondary GWs and their upward reflection at $z \sim 120$ km are clearly visible at $\Delta T = 115$ – 165 min. Note that near the F peak (at $z \sim 250$ km), the neutral wind perturbations above the body force are Sward for all 3 times, in the same direction as the body force.

[41] In Figure 15, we show the meridional wind perturbation, v , near the center of the body force at $z = 183$ km as a function of time. We see that the meridional wind perturbation is always negative (i.e., in the direction of the forcing), and is large. It increases rapidly with time at $\Delta T = 24$ min. Its maximum value is $v \sim -165$ m/s at $\Delta T = 50$ min, when the force is maximum. Thereafter, v decreases fairly rapidly in time to $v \sim -50$ m/s at $\Delta T = 80$ min. For $\Delta T > 80$ min, v decreases more slowly in time, reaching 5% of its maximum value at $\Delta T \sim 300$ min (~ 4 h after t_{\max}), and asymptoting to $v \sim 0$ m/s at $\Delta T \sim 400$ – 500 min (~ 6 – 8 h after t_{\max}).

5.1.1.2. Comparison With Neutral, Nonviscous Solutions

[42] Many of the general features of Figures 11–15 can be understood in terms of neutral, nonviscous, fluid dynamics. A horizontal body force accelerates the nonviscous neutral fluid, thus creating a neutral wind in the direction of the body force with spatial scales that are similar to the scales of the force if the parallel and perpendicular extents are similar (V2003). This is seen clearly in Figures 13 and 14. In fact, the horizontal flow and return flow in Figure 13 look quite similar to the nonviscous flow (V2003). Additionally, a horizontal body force in a nonviscous fluid excites upward and downward propagating secondary GWs (VF2001; V2003). These secondary GWs propagate as antisymmetric, concentric rings away from the body force. The GWs with the largest amplitudes propagate in the direction of and in the opposite direction of the body force. Because of the antisymmetric nature of the concentric rings, none of the GWs propagate perpendicular to the force direction. Finally, the amplitudes of the GWs in and against

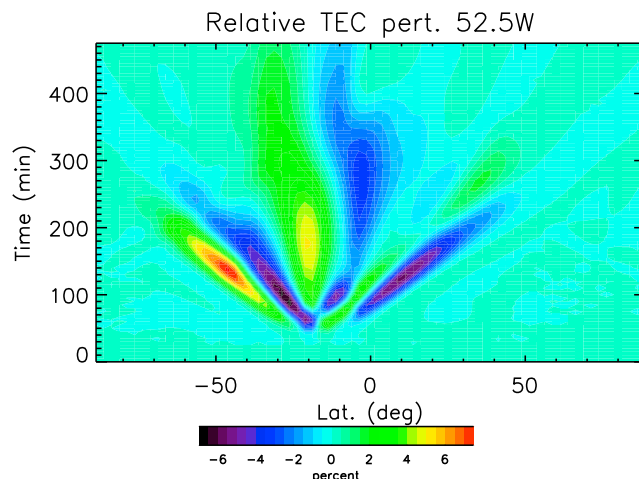


Figure 18. Relative TEC (in %) at 52.5°W as a function of latitude and time.

the direction of the force are equal, provided the background (and induced) winds are negligible (V2003). The peak λ_H of the GW spectrum is twice the width of the forcing, and the peak λ_z of the GW spectrum is 1–2 times the depth of the forcing if the forcing is reasonably fast (V2003). The secondary GW spectrum is broad, with significant amplitudes for GWs with λ_H (and λ_z) that are $\sim 1/4$ –10 times the value of λ_H (and λ_z) at the spectral maximum.

[43] A “slow” forcing generates negligible GWs, while a “fast” forcing efficiently generates GWs (VF2001). Although a continuous spectrum of GWs with periods larger than the buoyancy period of $\tau_b = 2\pi/N$ are excited from a horizontal body force in a nonviscous fluid, the spectrum is maximum at a wave period determined by its spatial and temporal characteristics. We neglect scale height effects, because $L_z \ll 4\pi H$ ($H \sim 24$ km at $z = 180$ km). Then the characteristic wave period of a horizontal body force, τ_c , is determined by replacing λ_x by $L_{x'}$, λ_y by $L_{y'}$ and λ_z by L_z in equation (1) (VF2001):

$$\tau_c = \frac{2\pi}{N} \sqrt{\frac{1/L_{x'}^2 + 1/L_{y'}^2 + 1/L_z^2}{1/L_{x'}^2 + 1/L_{y'}^2}}. \quad (19)$$

The force is fast if $L_t \ll \tau_c$, and is slow if $L_t \gg \tau_c$. If the force is fast, the GW spectrum peaks at the wave period $\tau_{\max} \sim \tau_c$. If the force is slow, $\tau_{\max} \sim (1-2)L_t$. If $L_t \sim (1-2)\tau_c$, then $\tau_{\max} \sim (1.2-2)\tau_c$.

[44] Let us compare these nonviscous solutions with our results here. For the body force parameters listed in equation (17) with $N = 0.016 \text{ s}^{-1}$ at $z = 180$ km, we calculate $\tau_c \sim 30$ min from equation (19). Therefore, the nonviscous, secondary, GW spectrum excited from this thermospheric body force is expected to peak at $\tau_{\max} \sim (1.2-2)\tau_c \sim 40$ –60 min. This is close to (although somewhat smaller than) the observed period of $\tau_r \sim 80$ min in Figures 11 and 12.

[45] Using the body force parameters in equation (17), the peak of the nonviscous secondary GW spectrum is expected to be $\lambda_H \sim 800$ –1300 km. Additionally, GWs with λ_H as small as $\lambda_H \sim 200$ km should also be excited. However, there is a lack of GWs with $\lambda_H < 2000$ km at any time in Figure 11. This is because of model resolution; the zonal and meridional grid points are separated by $\Delta_H \simeq 270$ km in the 2.5° TIME-GCM at this altitude and location. Assuming that 4 points are needed to represent a wave, this model cannot excite secondary GWs with $\lambda_H < 4\Delta_H = 1100$ km. For those secondary GWs with larger λ_H , only those with $\lambda_H \geq (9-10)\Delta_H \sim 2400$ –2700 km are adequately resolved, because of numerical damping. It is also possible that secondary GWs with $\lambda_H \sim 200$ –2000 km are excited, but are viscously dissipated below $z = 250$ km. However, ray trace studies have shown that many GWs with $\lambda_H > 100$ km and $\lambda_z > 100$ km can propagate up to $z = 250$ km prior to dissipating (see Figures 6b and 6d from V2007). Therefore, the likely cause for the monochromatic appearance of the secondary GWs in Figure 11 is the large horizontal resolution and numerical dissipation in the TIME-GCM. Using $\tau \sim 40$ –60 min and $\lambda_H \sim 800$ –1300 km, if we had not been resolution-limited, secondary GWs with $c_H \sim 100$ –600 m/s would likely have been excited. A higher-resolution study needs to be

performed to better determine the excited secondary GW spectrum from this thermospheric body force.

[46] Although the amplitudes of the upward and downward propagating, secondary GWs are equal in the Boussinesq approximation (V2003), in the thermosphere, the amplitudes of the upward propagating GWs increase with altitude while those of the downward propagating GWs decrease with altitude. This occurs because GW perturbation quantities such as T'/\bar{T} and v are proportional to $1/\sqrt{\bar{\rho}} \propto \exp(z/2H)$, since $\bar{\rho} \propto \exp(-z/H)$ [Hines, 1960]. This is clearly seen in Figure 12; the amplitudes of the downward propagating GWs ~ 40 km below z_{\max} are smaller than that of the upward propagating GWs ~ 40 km above z_{\max} . Additionally, except near the reflection altitude at $z \sim 120$ km, the slopes of the wave phase lines increase (decrease) above (below) $z_{\max} = 180$ km in Figure 12. This occurs because λ_z increases with altitude since \bar{T} increases with altitude (V2007). At $\Delta T \sim 115$ min, we estimate $\lambda_z \sim 25$ –30 km at $z \sim 150$ km and $\lambda_z \sim 370$ –390 km at $z \sim 250$ km for the secondary GWs. Here, we estimate λ_z by setting $\exp(i(\lambda_y + mz))$ constant along wave phase lines at constant x and t , so that $\lambda_z = \lambda_H \frac{dz}{dy} \Big|_{x,t}$. Therefore, λ_z is much smaller for the downward propagating GWs at $z \sim 150$ km than for the upward propagating GWs at $z \sim 250$ km.

[47] We also note from Figure 12 that the GW amplitudes are approximately constant with altitude for $z > 250$ km, and are large up to the top of the TIME-GCM at $z = 420$ km at $\Delta T = 165$ min. From Figure 9a of V2007, a GW with $\lambda_z \sim 350$ –400 km has a dissipation altitude of $z_{\text{diss}} \sim 350$ km, where z_{diss} is defined as the altitude where a GW’s momentum flux is maximum. But because a GW’s amplitude is significant $(1-2)H$ above z_{diss} (V2007), we estimate that the wave’s amplitude will be significant up to $z \sim 420$ –470 km. This is consistent with Figure 12.

[48] We now estimate $|\rho'/\bar{\rho}|$ from Figure 12 at $z \sim 400$ km. From the anelastic, dissipative polarization relations (VF2005, equations (B6) and (B7)),

$$\frac{\rho'}{\bar{\rho}} = -\frac{T'}{\bar{T}} \frac{(1 + i/2mH)}{(1 - i/2mH)}, \quad (20)$$

where primes denote perturbation quantities. For $1/2mH \ll 1$, equation (20) yields

$$\frac{|\rho'|}{\bar{\rho}} \sim \frac{|T'|}{\bar{T}}. \quad (21)$$

This is a fair approximation for these GWs. From Figure 12, the largest temperature perturbations of the GWs at $z \sim 400$ km are $T' \sim 30$ K. Since $\bar{T} \sim 825$ K, this yields $|\rho'/\bar{\rho}| \sim |T'/\bar{T}| \sim 3.6\%$. Because the GWs at the peak of the spectrum are not adequately resolved in this study, and because we estimate the momentum fluxes to be ~ 2 times larger at the maximum (V2003), it is probable that the temperature perturbation amplitudes of the excited secondary GWs with $\lambda_H \sim 800$ –1300 km would be 50% larger than their values at $\lambda_H \sim 2100$ –2200 km. We thus estimate maximum secondary GW amplitudes at $z \sim 400$ km as large as $|\rho'/\bar{\rho}| \sim 5\%$ for a single convective plume.

[49] As noted from Figures 12 and 14, the downward propagating GWs reflect upward at $z \sim 120$ km. For example, upward wave reflection is apparent at $\Delta T \geq$

90–115 min at $\sim(30\text{--}40)^\circ\text{S}$ and at $\sim(0\text{--}10)^\circ\text{S}$ in Figure 12. This occurs because the sound speed is less than the wave phase speed below this altitude, and a GW cannot propagate in a region of the atmosphere where its phase speed is greater than the sound speed. The Sward and Nward propagating GWs which move upward initially have negative and positive temperature perturbations, respectively, whereas the Sward and Nward propagating GWs which move downward initially (and reflect upward at $z \sim 120$ km) have positive and negative temperature perturbations, respectively. Indeed, in Figure 12 at $\Delta T = 165$ min, the initially upward and Sward propagating GWs can be seen at 45°S with $T' \sim -6$ K (black contour), whereas the initially downward and Sward propagating GWs which reflect upward at $z \sim 120$ km can be seen at 60°S with $T' \sim 4$ K (white contour). Therefore, the negative and positive ring patterns seen in Figure 11 consist of both the initially upward and downward propagating GWs. Because the amplitudes of the reflected GWs grow with altitude for $z > 120$ km, their amplitudes would equal their initial amplitudes once they reach $z \sim 180$ km assuming perfect reflection, neglecting geometric attenuation. Geometric attenuation causes the wave amplitudes to be somewhat smaller than their initial amplitudes, because the waves occupy a slightly larger area when they rereach $z \sim 180$ km. Additionally, the waves are dissipated somewhat as they propagate from $z \sim 180$ to 120 km and back up to 180 km. Note that the amplitudes of the reflected waves are $\sim 1/2$ that of the amplitudes of the initially upward propagating GWs at $z \sim 300\text{--}400$ km in Figure 12. Therefore, these initially downward propagating secondary GWs contribute to the variability of the F region to a somewhat smaller degree as compared to the initially upward propagating secondary GWs, although their contributions arise at larger radii.

[50] We can use an imagery source argument to understand why the radius of the reflected wave is larger than that of the unreflected wave. The virtual “source” of the reflected wave of the thermospheric body force is at $z \sim 120 - (180 - 120) \sim 60$ km (assuming that the wave reflects at $z \sim 120$ km, and neglecting the decrease in sound speed below $z \sim 120$ km). For a given frequency/vertical wave number component, the radius of the ring at a higher altitude must be larger if the effective source altitude is lower.

[51] We now argue that the reflected concentric ring rereaches $z \sim 183$ km at $\Delta T = 165$ min in Figure 13, $30\text{--}40^\circ$ from the center of the body force (e.g., at 55°W and 50°S). From Figure 12, we estimate $\lambda_z \sim 25\text{--}30$ km at $z \sim 150$ km and $\Delta T \sim 115$ min. At the reflection altitude, $m^2 = 0$, or $\lambda_z = \infty$. This increase in λ_z can be seen in Figure 12 at $\Delta T = 115$ min at $z \sim 130$ km. We therefore estimate an average vertical wavelength of $\bar{\lambda}_z \sim 60\text{--}100$ km at $z \sim 120\text{--}180$ km. Assuming that dissipation and winds are negligible, the estimated average vertical group velocity is $\bar{c}_{g,z} \sim -\bar{\lambda}_z/\tau_{Ir} \sim 13\text{--}21$ m s $^{-1}$ from equation (8). Assuming that $\bar{c}_{g,z}$ is approximately constant with altitude, the time taken for a GW to travel from $z = 180$ to $z \sim 120$ km and back to $z = 180$ km is $\sim 95\text{--}155$ min. Since the body force is maximum at $\Delta T = 45$ min, this means that the initially downward propagating GWs are predicted to rereach $z = 180$ km at $\Delta T \sim 140\text{--}200$ min. This is consistent with the presence of the outer concentric ring in Figure 13 at $z \sim 183$ km.

[52] We now compare the induced “mean” wind in Figure 15 with the induced neutral wind in a nonviscous fluid. When the body force is maximum, the induced mean zonal wind in a nonviscous fluid is 50% of its final value; it reaches its final value when the body force is finished (VF2001). In the thermosphere, a similar horizontal “mean” wind perturbation is also created from a horizontal thermospheric body force (see Figure 13). However, Figure 15 shows that v is maximum when the body force is maximum, with a maximum amplitude of $v \sim -165$ m/s. Thereafter, v decays rapidly, reaching 5% of its value ~ 4 h after t_{max} . Because v was plotted at a TIME-GCM grid point $\sim 1.05^\circ \sim 116$ km south of the center of the body force in Figure 15, and the spatial characteristics of the mean wind is similar to the spatial characteristics of the body force (V2003), the estimated meridional wind perturbation at the center of the body force is predicted to be

$$v_{\text{max}} \sim -165 \text{ m s}^{-1} / \exp(-116^2/(2 \times 89^2)) \sim -(370 - 400) \text{ m/s}. \quad (22)$$

Here we have used $\sigma_x \sim 400/4.5 \sim 89$ km. This is a very large wind perturbation, much larger than the background wind at this location and time (see Figure 10a). From neutral, nonviscous theory, the mean wind attained when $t - t_0 = L_t/2$ is (V2003)

$$\int_{t_0}^{t_0+L_t/2} F_0 f(t) dt = \frac{F_0}{2} \int_{t_0}^{t_0+L_t/2} \left[1 - \cos\left(\frac{2\pi(t-t_0)}{L_t}\right) \right] dt = \frac{F_0 L_t}{4} \quad (23)$$

using equation (16). Using equation (17), we estimate the neutral, nonviscous mean wind at $t - t_0 = L_t/2$ to be ~ 820 m/s for this body force. Therefore, the estimated value at the maximum, $v \sim -(370\text{--}400)$ m/s, is only $\sim 1/2$ of the value estimated from neutral nonviscous theory. This is likely because of viscous dissipation.

[53] After the body force is maximum in the thermosphere, $|v|$ decreases rapidly, reaching $\sim 30\%$ of its maximum value ~ 40 min later in Figure 15. Thereafter, the “mean” wind perturbation continues to be damped, but at a slower rate. This is in contrast to the nonviscous solution, where the induced mean wind is approximately constant in time after the body force is finished.

[54] We can estimate the dissipation rate in the thermosphere of the generated “mean” horizontal wind. We first assume that the “mean” wind perturbation varies as

$$\bar{v} = \bar{v}_0 \exp(-t/d) \exp\left(-\frac{(x-x_0)^2}{2\psi_x^2} - \frac{(y-y_0)^2}{2\psi_y^2} - \frac{(z-z_0)^2}{2\psi_z^2}\right), \quad (24)$$

where \bar{v}_0 is the value of \bar{v} at (x_0, y_0, z_0, t_0) , and d is the time scale for decay. Neglecting nonlinear effects and pressure divergences associated with vertical flows, the deceleration of this wind from kinematic viscosity is

$$\frac{\partial \bar{v}}{\partial t} \simeq \nu \nabla^2 \bar{v}, \quad (25)$$

where $\nabla^2 \equiv \partial^2/\partial x^2 + \partial^2/\partial y^2 + \partial^2/\partial z^2$. Substituting equation (24) into equation (25), and evaluating the result at the location

where the wind is the strongest (i.e., at (x_0, y_0, z_0)), the time scale for decay is [Vadas and Nicolls, 2009]

$$d \simeq \nu^{-1} \left(\frac{1}{\psi_x^2} + \frac{1}{\psi_y^2} + \frac{1}{\psi_z^2} \right)^{-1}. \quad (26)$$

Since the vertical variation of the created neutral wind is smaller than the horizontal variation, the decay time scale is simply $d \simeq \psi_z^2/\nu$. Taking into account the increase of the dissipation rate because of thermal diffusivity, we estimate

$$d \simeq \psi_z^2 / [\nu(1 + \text{Pr}^{-1})]. \quad (27)$$

If we assume a full vertical depth of the created wind perturbation of ~ 86 km from equation (17) and Figure 14, then $\psi_z \simeq 86/4.5 \simeq 19.1$ km. Using $\nu \simeq 5.76 \times 10^4$ m²/s at $z \sim 184$ km, equation (27) yields $d \sim 44$ min. Therefore, the created neutral wind perturbation at $z \simeq 184$ km is predicted to decrease to 37%, 14%, and 5% of its initial value after ~ 44 min, ~ 88 min and ~ 132 min, respectively, because of kinematic viscosity and thermal diffusivity. Because the body force peaks at $\Delta T = 45$ min with $v \sim -165$ m/s, we predict the mean meridional wind perturbation to be -61 , -23 , and -8 m/s at $\Delta T = 89$, 133, and 180 min, respectively. From Figure 15, the meridional wind perturbation is $v \sim -61$, -23 , and -8 m/s at $\Delta T = 75$, 135, and 300 min, respectively. These times are close to the predicted values, especially for the first few hours. We conclude that the created “mean” horizontal wind decays rapidly in Figure 15 mainly because of kinematic viscosity and thermal diffusivity. However, other dissipative effects, such as back-pressure and geostrophic (or gradient-wind) adjustment may also be relevant in causing the mean wind to decrease in time.

[55] Finally, the average horizontal wind at t_{max} in the body force region is estimated to be relatively large, $\bar{v}_{\text{max}}/2 \sim 125$ – 165 m/s, which is much larger than the background wind at this time (see Figure 5). It is, however, smaller than the horizontal phase speed of the large-scale secondary GWs that are excited from the body force. This is the reason there is virtually no asymmetry in the amplitudes of the GWs propagating Sward and Nward in Figure 11. If the created wind in the force area had been much larger, then the excited secondary GWs propagating Sward would have had larger amplitudes at higher altitudes than the GWs propagating Nward, because λ_z would have been larger for the Sward propagating GWs, thereby resulting in higher dissipation altitudes. This is because although the intrinsic frequencies for the Sward and Nward GWs are equal in the frame moving with the induced “mean” wind, the ground-based frequencies,

$$\omega_r = \omega_r + l v, \quad (28)$$

are larger for the Sward propagating GWs as compared to the Nward propagating GWs. Therefore, after propagating outside the body force region, since ω_r is approximately constant along a ray path [Lighthill, 1978], the Sward propagating GWs have larger intrinsic frequencies than the Nward propagating GWs. This causes λ_z to be larger for the Sward propagating GWs, which increases z_{diss} . This effect depends on the value of $|v|$; the larger $|v|$ is, the more

strongly asymmetric are the amplitudes of the Sward and Nward propagating GWs at higher altitudes.

5.1.2. Global Response

[56] We now investigate the global response to the body force in more detail. Figure 16 shows T' at $z = 250$ km as a function of latitude and time on the nightside at 52.5°W , close to the center of the body force. The center of the body force appears as a dipole, with a maximum at $\Delta T \simeq 65$ min. The global propagation of large-scale secondary GWs away from the body force is clearly seen in Figure 16. Because of their large horizontal phase speeds, these GWs reach the south and north poles at $\Delta T = 300$ and 400 min, 4 h and 6 h after t_{max} , respectively. The ability of large scale, long period, high phase speed GWs to propagate large horizontal distances on the nightside before dissipating is a well-known phenomenon [Richmond, 1978; Walker et al., 1988; Hocke and Schlegel, 1996]. Note that the GW amplitudes at the south and north poles are much smaller than initially because of geometric attenuation. Additionally, there is a small positive temperature perturbation near the south pole at $\Delta T \sim 140$ min, which moves Nward in time. This is due to numerical instability from the wavenumber filter for the high-resolution TIME-GCM, and does not affect the main results of this study.

[57] Figure 17 shows the relative atomic oxygen [O] density perturbation at $z = 300$ km and 52.5°W as a function of latitude and time. As before, large-scale GWs are seen propagating away from the thermospheric body force. We see that the amplitudes of the relative [O] perturbations are as large as $\sim 2\%$. Since we are not resolving the peak of the secondary GW spectrum, the GW perturbation amplitudes are likely underestimated by 50%. We thus estimate the amplitude of the relative [O] perturbations from the secondary GWs at the spectral peak to be as large as $\sim 2.5\%$.

5.2. Plasma Response

[58] Figure 18 shows the relative total electron content (TEC) perturbations as a function of latitude and time. Here, the TEC is the vertical integration of the electron densities. We see that the electrons respond locally and globally to the passage of the large-scale GWs and to the body force, as expected [Klostermeyer, 1972; Kirchengast et al., 1996]. Sward and Nward of the forcing, LSTIDs with amplitudes as large as 8% are seen propagating away from the body force at the same times and latitudes as the T' or relative [O] perturbations from Figures 16 and 17, respectively. Therefore, Figure 18 shows that large-scale LSTIDs are created by the propagation of the excited, large-scale, secondary GWs.

[59] Figure 18 also shows that the created TEC perturbations are somewhat more complicated than the T' or [O] perturbations shown in Figures 16 and 17. North of the magnetic equator at 0 – 10°N , 55°W , and $z \sim 183$ km, the neutrals move Sward at $\Delta T = 115$ min (see Figure 13). Because of the neutral-ion collisions which create ion drag, the neutrals “drag” the F region ions Sward with them. However, since the ions are constrained to move along the magnetic field lines, which decrease with altitude away from the magnetic equator, the ions and electrons move Sward and upward. The upward motion of the electrons decreases the electron density perturbation. This decrease is seen at 0 – 10°N at $\Delta T = 115$ min as a -4% perturbation in Figure 18. In contrast, the ions south of the magnetic

Table 1. Body Force Parameters

Time (UT)	$L_{x'}$ (km)	$L_{y'}$ (km)	L_z (km)	L_t (hr)	F_0 (m s^{-2})	lon_{max} (deg)	lat_{max} (deg)	z_{max} (km)	t_{max} (hr)	θ (deg)	z_{opp}/H
0	410	590	80	1.2	1.0	-50.9	-14.1	180	1.08	17	1.3
3	380	560	55	0.82	1.1	-50.9	-14.1	164	4.08	22	1.8
6	410	520	50	1.2	0.5	-51.4	-13.6	148	7.25	38	1.9
9	360	360	50	0.43	0.6	-51.8	-13.6	156	11.08	44	2.4
12	430	660	95	1.1	0.8	-50.9	-15.9	176	13.25	-20	1.4-2.2
15	410	650	90	0.90	1.1	-50.9	-15.9	176	16.25	-21	1.7-2.4
18	360	440	95	0.95	0.5	-50.5	-14.1	180	19.08	19	1.8-2.8
21	390	560	80	0.70	0.9	-53.2	-17.7	176	22.58	-89	2.4
24	410	610	75	0.49	0.7	-52.3	-18.6	188	25.75	-77	3.0

equator at 40–50°S are dragged Sward by the neutrals at $\Delta T = 115$ min (see Figure 13). The electrons respond to the ion movements by moving Sward and downward, thereby increasing the electron density perturbations. This is also seen in Figure 18 at 40–50°S at $\Delta T = 115$ min as a 5% perturbation.

[60] In addition to the response of the plasma to the secondary GWs, seen as LSTIDs in the TEC, there is also a TEC perturbation at the location of the body force. In particular, we see a large positive TEC perturbation near the location of the body force at 18°S in Figure 18. This perturbation is caused, at least in part, by the reaction of the electrons to the neutral wind created by the body force. From Figure 13, the central portion of the neutral flow at 55°W and 18°S is Sward. This is also true at higher altitudes as well (see Figure 14). Therefore, the electrons at 18°S move downward because of ion drag, causing the electron density to increase. This is what is observed in Figure 18 at 18°S and $\Delta T = 100$ –400 min. Thus, this TEC perturbation appears to be caused, in part, by the “mean” neutral wind perturbation induced by the body force. However, the TEC perturbation is long-lived, lasting for ~ 7 h with significant amplitudes, long after the neutral wind perturbation has decayed away (see Figure 15). Therefore, the plasma response above the body force lasts much longer than the neutral response. We will delve into the plasma response to thermospheric body forces further in a future paper.

6. Daily Variability of the Thermospheric Body Forces

[61] As we saw in Figure 10b, the winds at $z \sim 120$ km dictate the direction of the thermospheric body force created from the convective plume shown in Figure 1. But from Figure 4, the variability of the zonal wind at this altitude is complicated, and includes diurnal and semidiurnal tides, and other wave components. We therefore calculate the body forces which result from the dissipation of GWs excited from this same convective plume, but which overshoots the tropopause at the same location every 3 h from $t = 0$ to 2400 UT. The results are shown in Table 1. From left to right, Table 1 shows the time of convective overshoot (in UT), $L_{x'}$ (in km), $L_{y'}$ (in km), L_z (in km), L_t (in hours), F_0 (in m s^{-2}), lon_{max} (in degrees), lat_{max} (in degrees), z_{max} (in km), t_{max} (in fractions of an hour), θ (the angle of the body force counterclockwise from east) (in degrees), and z_{opp}/H (where H is calculated at z_{max}). In the last column, we show several values if the wind is opposite to the body force direction at several altitudes. We see that the body force maxima are directed SEward, NEward, or Sward. They are not directed Wward,

because the winds in the lower thermosphere are Wward at this location and time (see Figure 4a). Additionally, the body forces have parallel widths of $L_{x'} \sim 300$ –500 km, perpendicular widths of $L_{y'} \sim 300$ –700 km, depths of $L_z \sim 50$ –100 km, durations of $L_t = 30$ –80 min, and magnitudes of $F_0 \sim 0.5$ –1.1 m s^{-2} . The altitudes where the body forces are maxima range from $z_{\text{max}} = 140$ to 190 km. The times the body forces are maxima ranges from 1.1 to 2.1 h after convective overshoot. Finally, we see that the winds are typically opposite to the body force direction (1.5–2.5) H below z_{max} . This occurs because H sets the vertical scale over which GWs dissipate (VF2005; V2007).

[62] Table 1 shows that significant thermospheric body forcing occurs 1–2 h after convective overshoot. Because these body forces have large widths, they are predicted to excite large-scale, secondary GWs with $\lambda_H \sim 200$ –5000 km and with periods of 20 min to a few hours (V2003). Those secondary GWs with large phase speeds, long periods, and large horizontal scales will propagate globally on the night-side. Therefore, the excitation of large-scale GWs is likely a significant contributor of thermospheric variability during the seasons when deep convection occurs.

[63] Figure 19 shows horizontal slices at z_{max} and t_{max} for the thermospheric body forces created from the plumes from Table 1. While the body force changes direction and intensity throughout the day, it is predominantly Eward, NEward, Sward, or SEward. None of the body forces are Wward. Therefore, the body forces do not rotate counterclockwise with the diurnal tides, although they are certainly influenced by the diurnal cycle. Because the body force direction varies throughout the day, the direction of propagation of the excited secondary GWs and LSTIDs vary throughout the day. On this day, for example, the largest-amplitude LSTIDs propagate Eward and Wward at 0000 UT, NEward and SWward at 0300, 0600, 0900, and 1800 UT, SEward and NWward at 1200 and 1500 UT, and Sward and Nward at 2100 and 2400 UT. However, secondary GWs are excited in all directions except that perpendicular to the body force direction. Thus, secondary GWs propagate in all directions throughout the day.

[64] Figure 20 shows vertical slices of the thermospheric body forces from Table 1. For each plume, we show the body force every 10 min at lon_{max} and lat_{max} . In general, the generated body force moves upward in time, and only typically lasts for 30–60 min.

7. Discussion of Observations Supporting This Mechanism

[65] In this paper, we found that large-scale, globally propagating secondary GWs and LSTIDs with $\lambda_H \sim$

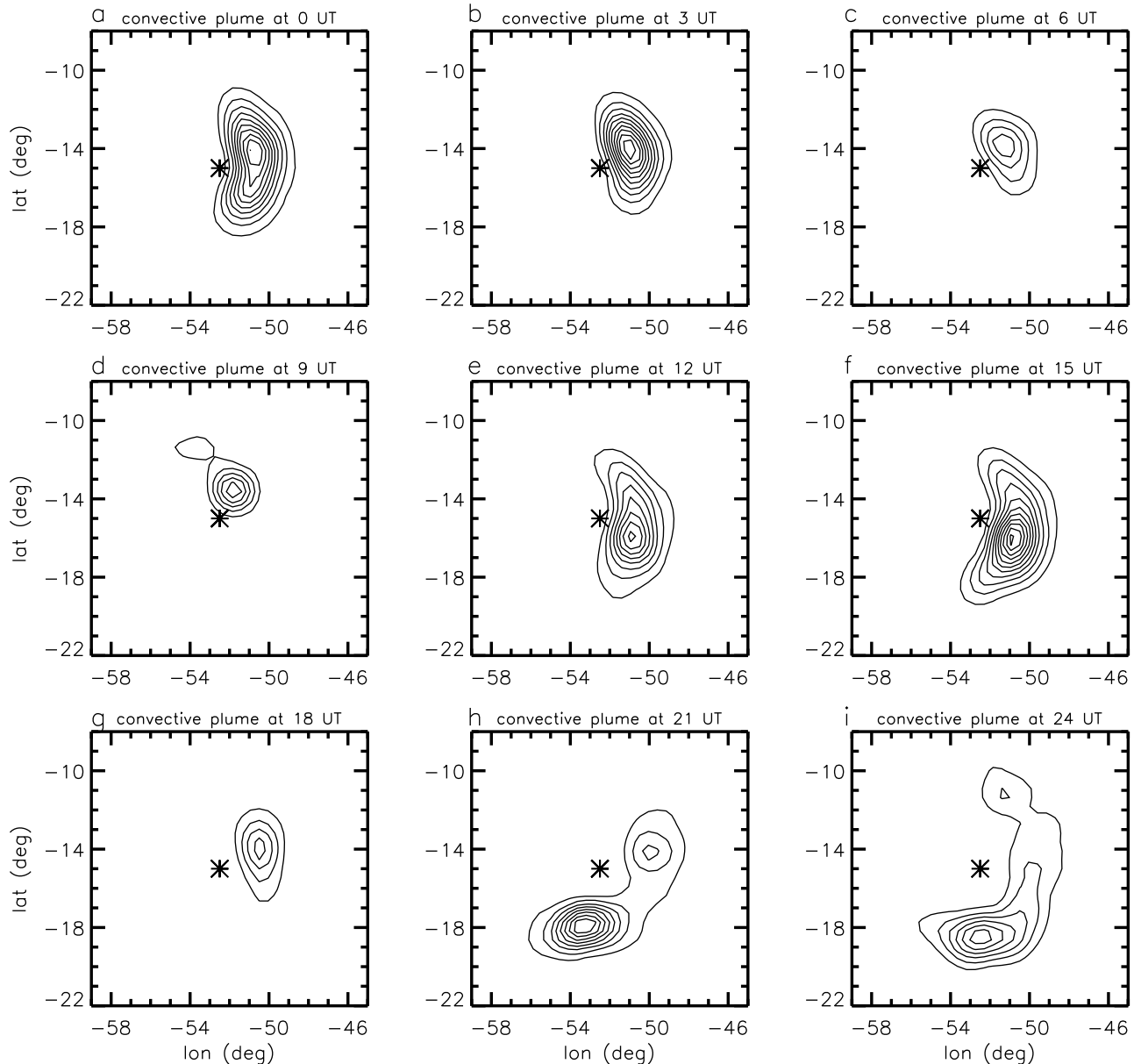


Figure 19. Horizontal slices of the body forces at the times and altitudes where they are maximum (see Table 1). We show the slices for the convective plumes which overshoot the tropopause at (a) 0000, (b) 0300, (c) 0600, (d) 0900, (e) 1200, (f) 1500, (g) 1800, (h) 2100, and (i) 2400 UT. Contours are shown in intervals of 0.1 m s^{-2} . Asterisks show the location of the convective plume.

2100–2200 km are generated from a thermospheric body force. This body force was created from the dissipation of small- and medium-scale GWs excited from a deep convective plume. This process represents a fundamental and important dynamical mechanism in the thermosphere that has not been investigated previously. Because most of the convectively generated, primary GWs propagate locally only up to $z \sim 120\text{--}250$ km, and because the secondary, large scale GWs propagate globally up to at least ~ 420 km, this process therefore facilitates the “upward cascade” of energy and momentum from small scales in the troposphere to large scales at high altitudes in the thermosphere. Additionally, because thunderstorms and deep convection are an every day occurrence during the spring, summer and fall months in

many parts of the world, this process therefore likely creates a nearly continuous supply of large-scale GWs in the thermosphere during these seasons, regardless of geomagnetic activity.

[66] The mechanism discussed in this paper resolves a decades-old mystery as to the source of large-scale GWs and LSTIDs in the thermosphere during geomagnetically quiet times, especially near the equator. Indeed, perturbations in the atomic oxygen density [O] with large scales of $\lambda_x, \lambda_y \sim 400\text{--}4000$ km have been observed during low magnetic activity with the DE2 satellite at $z \sim 300$ km [Hedin and Mayr, 1987], and large-scale GWs have been observed during quiet geomagnetic conditions [Mayr et al., 1990]. Forbes et al. [1995] observed large-scale density

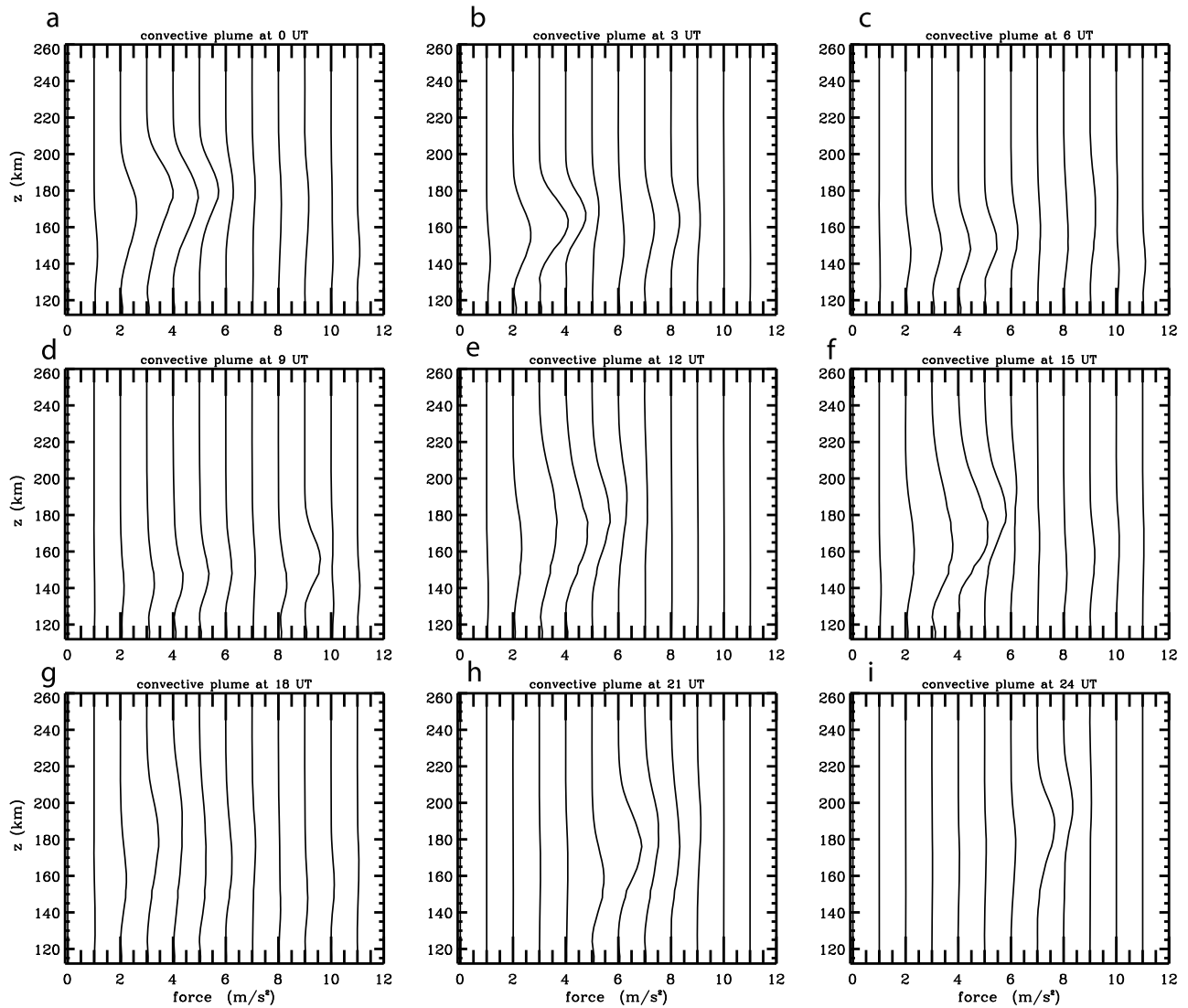


Figure 20. Vertical slices of the body forces at the locations where they are maximum (see Table 1). We show the slices for the convective plumes which overshoot the tropopause at (a) 0000, (b) 0300, (c) 0600, (d) 0900, (e) 1200, (f) 1500, (g) 1800, (h) 2100, and (i) 2400 UT. Profiles are shown every 10 min from 35 to 145 min after convective overshoot and are offset by 1.0 m s^{-2} .

perturbations at $z \sim 200$ km during quiet geomagnetic conditions with λ_H as large as 2500 km. *Bruinsma and Forbes* [2008] observed large-scale density perturbations at $z \sim 400$ km using the CHAMP satellite during quiet geomagnetic conditions with λ_H as large as 2400 km. *Bruinsma and Forbes* [2008] found that during quiet or active geomagnetic activity, the average RMS of the relative density perturbations are approximately the same at equatorial latitudes during the daytime for all medium and large-scale waves. Because small- and medium-scale waves cannot propagate to the equator from the auroral zone [*Richmond, 1978*], and because large-scale waves from the auroral zone cannot propagate to the equator during the daytime because of ion drag and relatively large ion densities [*Hajkowicz, 1990; Tsugawa et al., 2003*], daytime measurements effectively eliminate the aurora as a source of large-scale waves at the equator. Therefore, these studies show that there is a source of medium- and large-scale waves near the equator

that is independent of auroral (Joule) heating. Indeed, *Forbes et al.* [1995] wrote, “A significant result to emerge from this study... is the recognition that the lower thermosphere is virtually always characterized by wavelike structures in the density field (of order 10–40% peak to peak), even during geomagnetically quiet periods.”

[67] For waves with long wavelengths (i.e., of $\lambda_x, \lambda_y \sim 400\text{--}4000$ km) near the magnetic equator, *Hedin and Mayr* [1987] found the quiet time DE2 satellite [O] perturbations to be $\sim 2\%$ at $z \sim 300$ km. In this paper, we estimated the [O] perturbations from the secondary GWs to be as large as $\sim 2\%$ at $z \sim 300$ km for a single deep convective plume. Thus, our model results are in good agreement with these measurements. Additionally, *Bruinsma and Forbes* [2008] found that during geomagnetically quiet conditions, the root-mean-square (RMS) of the density perturbations near the equator are sensitive to LT, being larger at night than during the day. For a similar temperature, latitude, and LT as

that modeled in this paper, they determined the RMS density perturbations to be 4–6% at $z = 370\text{--}450$ km. This compares well with our model results, as we found $|\rho'/\bar{\rho}|$ for the secondary GWs to be as large as $\sim 3.6\%$ at $z \sim 400$.

[68] Because the TIME-GCM did not resolve the peak of the excited secondary GW spectrum because of numerical damping, our model perturbation amplitudes were likely underestimated by 50%, as discussed in section 5. Therefore, we estimate the relative [O] perturbations to be as large as 2.5% at $z = 300$ km and $|\rho'/\bar{\rho}|$ to be as large as $\sim 5\%$ at $z = 400$ km for secondary GWs at the peak of the spectrum. Additionally, there are often many deep convective plumes within a convectively active area of $500\text{ km} \times 500\text{ km}$. Because the GWs created from each of these plumes encounter similar winds, the amplitude of the resulting thermospheric body force might increase; VF2006 showed that many deep convective plumes within a 100 km region increased the strength of the thermospheric body force by a factor of 2–3. This effect would increase the secondary GW amplitudes by a factor equal to the increase in the body force amplitude, leading to larger [O] perturbation and $|\rho'/\bar{\rho}|$ amplitudes. However, recent simulations that include parameterized GW breaking suggest that the maximum body force amplitude attainable is $\sim 1\text{ m/s}^2$ for multiple convective plumes (S. L. Vadas and H.-L. Liu, manuscript in preparation, 2009). Thus, the amplitudes calculated in this paper are likely representative of secondary wave amplitudes from multiple convective plumes.

[69] *Forbes et al.* [1995] determined the GW density perturbation spectrum at $z \sim 200$ km during May–August in the northern hemisphere for GWs with $\lambda_H \sim 150\text{--}2500$ km during quiet times geomagnetically. They found that the power spectral density (PSD) increases approximately asymptotically with horizontal wavelength up to $\lambda_H \sim 2300$ km, then decreases somewhat for larger wavelengths. Our model results are consistent with these measurements, and explain the likely origin of these large-scale waves. At this altitude, we expect the waves to be a mixture of upward propagating GWs (that have not yet dissipated) plus excited secondary GWs generated from thermospheric body forces (from wave dissipation at $z \lesssim 200$ km). The fact that the GW spectrum is broad is consistent with nonviscous neutral theory (V2003). The fact that the spectrum appears to peak at $\lambda_H \sim 2300$ km can be understood if we correct for the fact that the satellite was likely not aligned with the wave propagation direction for most of these waves, thereby resulting in an overestimate of λ_H .

[70] *Shibata* [1986] analyzed daytime HF Doppler measurements in Japan from 4 sites, and found that 2 distinct types of waves were seen near the F peak. The first, waves with $c_H \leq 300\text{ m s}^{-1}$, nearly all propagated in the SEward direction. The second, waves with $c_H > 300\text{ m s}^{-1}$, propagated in nearly all directions azimuthally. Because GWs with $c_H > 300\text{ m s}^{-1}$ cannot originate in the lower atmosphere, and because nearly all of the high phase speed waves are propagating in directions other than Sward, most of these high phase speed waves must be created from a process which does not involve auroral heating. We suggest that these waves are likely the large-scale, secondary GWs that are excited from the dissipation of small- and medium-scale GWs below the F peak. These small- and medium-scale GWs can be from any lower atmospheric GW source. We

suggest this because the secondary GWs excited from thermospheric body forces are nearly omnidirectional and are estimated to have large phase speeds of $c_H \sim 100\text{--}600\text{ m s}^{-1}$ (see section 5). Most of the observed GWs with $c_H < 300\text{ m s}^{-1}$ are likely excited from lower atmosphere sources. Those slower waves which reach $z \sim 250$ km tend to propagate in the opposite direction of the wind because of dissipative filtering (V2007; FV2008); indeed, the thermospheric wind was estimated to be NWward at this location and time from a wind model [*Shibata*, 1986]. Note that the large-scale GWs are much less affected by the thermospheric winds because of their large phase speeds. For the fast GWs with $c_H > 300\text{ m s}^{-1}$, *Shibata* [1986] also found that there were significantly more waves having periods of 40 min than having periods of 20 min, and that there were few waves with periods of 13.3 min. This agrees with our model results as well, because we argued that the excited secondary GW spectrum from this thermospheric body force peaks at wave periods of $\tau_{\max} \sim (1.2\text{--}2)\tau_c \sim 40\text{--}60$ min (although likely because of numerical damping, the TIME-GCM simulation shown here results in a wave period of 80 min).

[71] Additionally, *Maeda and Handa* [1980] found that although LSTIDs over Japan were mostly Sward propagating during periods of large polar magnetic disturbances, “during the period of low magnetic activity the direction [of propagation of the LSTIDs] scatters considerably.” *Sharadze et al.* [1986] also found that many of the LSTIDs observed over the former Soviet Union were propagating in directions other than Sward. *Walker et al.* [1988] found several cases where the LSTIDs propagated Nward with periods of 70 min, although this could have been from auroral heating near the southern pole. The propagation of LSTIDs in a direction other than Sward in the northern hemisphere supports the mechanism discussed in this paper.

[72] Other evidence supports the existence of a source of waves and wave energy at $z \sim 200$ km. *Schlegel* [1986] reported a pronounced maximum of the wind parallel to the magnetic field line at an altitude slightly below 200 km that was difficult to explain. *Shibata and Schlegel* [1993] found an enhancement of wave power at $z \sim 180\text{--}210$ km, which they could not attribute to dissipating GWs. They also discovered a downward propagating wave(s) with a ~ 2 h period using band-pass-filtered EISCAT data during a period of relatively quiet geomagnetic activity. This wave(s) appeared to originate at $z \sim 180\text{--}200$ km at 0600 UT on 7 September 1998 and lasted for several cycles (~ 6 h). These observations were made along the magnetic field line, which is nearly vertical over northern Norway. Therefore, we deduce from Figure 9 of *Shibata and Schlegel* [1993] that $\lambda_z \sim 20\text{--}30$ km for the downward propagating GWs at ~ 0800 UT. This is very similar to our model results at $z \sim 115$ km, which is 70 min after the body force is maximum: $\lambda_z \sim 25\text{--}30$ km (see Figure 12). We estimate that the downward propagating GW observed by *Shibata and Schlegel* [1993] had $\lambda_H \sim 500\text{--}600$ km (assuming zero wind) using $N \sim 0.02\text{ s}^{-1}$ at this altitude. A secondary GW having this horizontal scale is expected to be excited by the thermospheric body force studied in this paper, although it was not resolved in this simulation because of numerical damping.

[73] Although *Shibata and Schlegel* [1993] suggested that wave reflection from a wind shear at $z \sim 200$ km caused the downward propagating GW, there does not appear to

be an upward propagating wave with a similar λ_z prior to 0600 UT. Additionally, there is evidence of a thermospheric body force and its rapid dissipation from viscous dissipation; Figure 11 of *Shibata and Schlegel* [1993] shows a large negative meridional wind of ~ 80 m/s which decelerates rapidly to zero within 1–1.5 h at $z \sim 200$ km. This deceleration is too rapid to be caused by the diurnal tide; it is better explained as the viscous damping of the generated “mean” neutral wind (see equation (27)). Indeed, we found that the generated “mean” neutral wind decreases to 13–14% of its maximum value ~ 90 min after this “mean” wind perturbation is maximum (see Figure 15). Finally, an upward propagating wave is also noticeable in their Figure 9 at and after 0700 UT up to their maximum altitude of $z \sim 240$ km. This wave has a larger λ_z than that of the downward propagating wave, consistent with our results. Therefore, our new mechanism is consistent with these measurements.

[74] *Shiokawa et al.* [2006] observed Sward moving GWs uncorrelated with the Kp index at $z \sim 200$ –300 km in Indonesia with $\lambda_H \sim 700$ km and $\tau_r \simeq 40$ min. Because these waves cannot propagate in the lower atmosphere, were most frequently observed in May–July, and the Asian monsoon is north of Indonesia, it is possible that small- and medium-scale GWs excited by the monsoon dissipated in the thermosphere, creating thermospheric body forces north of Indonesia at $z \sim 120$ –250 km. These body forces could then have excited large-scale secondary GWs with $\lambda_H \sim 700$ km which propagated in concentric rings away from the monsoon area; over Indonesia, these secondary GWs would then have been Sward propagating.

[75] Finally, a recent study using the Poker Flat Incoherent Scatter Radar (PFISR) found that the background, neutral wind accelerated in the SEward direction by ~ 100 –150 m/s over 30–40 min at $z \sim 190$ km [*Vadas and Nicolls*, 2009]. They also found horizontal spatial inhomogeneities of the neutral wind over 50–100 km. Because the accelerations and spatial inhomogeneities were not consistent with tides, and because there was strong wind flow over tall mountains NW of PF, they hypothesized that these accelerations were thermospheric body forces caused by the dissipation of SEward propagating GWs excited by mountain wave breaking near the mesopause at $z \sim 80$ km.

8. Conclusions and Discussions

[76] In this paper, we studied the response of the thermosphere and ionosphere to the dissipation of GWs excited by a single deep convective plume. This plume overshoot the tropopause on 1 October 2005 at ~ 2020 UT (~ 1 h prior to sunset), and was located at 52.5° W and 15.0° S. This plume had a horizontal extent and updraft velocity typical of deep convective plumes during this campaign. Using a convective plume model, we calculated the approximate GW spectrum excited by this plume. We then ray traced this spectrum upward into the atmosphere. Filtering from wind, temperature and viscous dissipation caused the primary GW spectrum to be oriented NEward and Sward when it reached $z \sim 160$ –200 km. The dissipation of the small- and medium-scale GWs in the spectrum created momentum flux divergence, which caused the background neutral wind to be accelerated in the direction of propagation of the dissipating GWs. The GWs most important for the creation of this thermospheric

body force had $\lambda_H \sim 40$ –150 km, $\lambda_z \sim 50$ –65 km, and $\tau_r \sim \tau_{r'} \sim 10$ –20 min. For this convective plume, the body force was created just after sunset, was predominantly Sward, was maximum at $z \sim 180$ km, had an amplitude of 1.3 m/s², had parallel and perpendicular full widths of 400 and 640 km, respectively, had a full depth of 85 km, and lasted for 40 min. We found that the direction of the body force was opposite to the background winds ~ 2 density scale heights lower, or at $z \sim 120$ km. Because the direction of the tides continue to rotate with altitude above $z > 120$ km, the body force was oriented in a similar direction as the neutral wind at $z \sim 180$ –250 km in this case. Thus, the body force did not “drag” or decelerate the neutral wind, as can be the case with GW breaking near the mesopause.

[77] We inserted the largest-amplitude portion of this body force into the high-resolution TIME-GCM, and found that upward and downward propagating, large-scale, secondary GWs were excited. These GWs were fairly monochromatic, with virtually no spectral variation, and propagated away from the body force in all directions except that perpendicular to the body force. They had horizontal wavelengths of $\lambda_H \sim 2100$ –2200 km, periods of $\tau_r \sim 80$ min, and phase speeds of $c_H \sim 480$ –510 m/s. The GWs with the largest amplitudes propagated Sward and Nward (with and against the direction of the body force, respectively), with temperature perturbation amplitudes as large as 3.6% at $z = 400$ km. Those Nward and Sward moving GWs propagated globally, reaching the south and north poles ~ 4 and ~ 6 h later, respectively. This global propagation was likely possible only because this longitude band was dark; indeed, large-scale GWs rapidly dissipate because of ion drag when propagating on the dayside [*Yeh et al.*, 1975; *Hajkowicz*, 1990; *Tsugawa et al.*, 2003]. Because the peak of the GW spectrum is expected theoretically to be at $\lambda_H \sim 800$ –1300 km and $\tau_r \sim 40$ –60 min instead, we noted that numerical dissipation in the TIME-GCM likely damped out all GWs with $\lambda_H < 2000$ km. If we had not been resolution-limited, secondary GWs with $c_H \sim 100$ –600 m/s would likely have been excited. Higher-resolution studies are needed to understand more fully the spectrum of secondary GWs excited by thermospheric body forces.

[78] We note that the sizes and speeds of the large-scale secondary GWs simulated here are comparable in size to those produced during geomagnetic storms from the auroral electrojet [*Lu et al.*, 2001]. These aurorally generated, large-scale waves also propagate globally during the nighttime, with horizontal speeds of ~ 500 –600 m/s [*Hajkowicz*, 1991; *Tsugawa et al.*, 2003].

[79] We also found that the excited, large-scale secondary GWs create (1) density perturbations as large as $\sim 3.6\%$ at $z \sim 400$ km and (2) [O] perturbations as large as $\sim 2\%$ at $z = 300$ km. Because the TIME-GCM did not resolve the peak of the excited secondary GW spectrum, we estimated that the peak values were 50% larger, or $|\rho'/\bar{\rho}|$ as large as $\sim 5\%$ at $z \sim 400$ km and relative [O] perturbations as large as $\sim 2.5\%$. These values agreed well with CHAMP and DE2 satellite measurements, respectively. Because small- and medium-scale GWs from the lower atmosphere do not typically propagate above $z \sim 300$ km [V2007; *Earle et al.*, 2008], we postulate that most of the waves observed during geomagnetically quiet conditions by *Hedin and Mayr* [1987], *Mayr et al.* [1990], and *Bruinsma and Forbes*

[2008] (i.e., at $z \geq 300$ km) were secondary GWs excited by thermospheric body forces that were created by the dissipation of small- and medium-scale GWs from the lower atmosphere.

[80] Additionally, we found that this body force created a “mean,” neutral, horizontal wind in the direction of the body force at altitudes of $z \sim 120$ – 250 km. This created large vertical wind shears at $z \sim 130$ – 160 km and at $z \sim 210$ – 250 km. Horizontal return flows were also induced, which created regions of oppositely directed neutral wind flow several hundred km horizontally from the body force. At the location of the body force, this induced wind was “spun-up” to an estimated amplitude of $v \sim -(370$ – $400)$ m/s within 20 min, which was the time for the body force to reach its maximum. This “mean” neutral wind was dissipated to 5% of its maximum value ~ 4 h later. We argued that this was likely due primarily to damping from kinematic viscosity and thermal diffusivity.

[81] Importantly, we found that this body force created LSTIDs in response to these large-scale GWs. These LSTIDs propagated on the nightside with TEC amplitudes as large as 8%, “following” the large-scale secondary GWs as they propagated globally. Additionally, at the location of the body force, a TEC perturbation was created with an amplitude of 8% which lasted for ~ 7 – 8 h after the forcing, well after the neutral response died away. This response appeared to be associated, in part, with the horizontal Sward flow induced by the thermospheric body force in this case.

[82] Finally, we argued that secondary GWs with $\lambda_H \sim 400$ km should be excited. Those GWs with $\tau_r \sim 30$ – 40 min would have $c_H \sim 160$ – 230 m s⁻¹, which is large enough to survive thermospheric dissipation at the excitation altitude (V2007). Therefore, although it is traditionally assumed that F region GWs with $c_H < 250$ – 300 m s⁻¹ are all from the lower atmosphere [e.g., Hocke and Schlegel, 1996], some of these GWs may also be secondary GWs created from thermospheric body forces.

[83] We also calculated the thermospheric body forces that resulted from the same convective plume, but that overshoot the tropopause every 3 h throughout the day. We found that the altitudes where the body forces are maximum range from $z_{\max} = 140$ to 190 km. This limited altitude range occurs because these body forces are created from kinematic viscosity and thermal diffusivity. Because v increases nearly exponentially with altitude, nearly all of the GWs in the initial convective spectrum are dissipated below $z < 250$ km (V2007). Additionally, we found that the direction, amplitude, and altitude of the created thermospheric body force change as a function of LT. However, because the GWs which contribute to the body force are dissipated at $z \sim 120$ – 250 , which is (1–2)H below the body force, and because the winds in the lower thermosphere are a combination of semidiurnal and diurnal tides and other waves, the body force does not rotate diurnally throughout the day. This is different from freely propagating GWs from the lower atmosphere at $z \sim 250$ km, which tend to propagate opposite to the winds at $z \sim 250$ km, and therefore have directions which vary diurnally [Waldock and Jones, 1986; Crowley et al., 1987]. Thus, accurate wind models in the lower thermosphere are necessary for an accurate understanding and quantification of thermospheric body forces. Additionally, because the body force direction varies throughout the day,

the excited secondary GWs and LSTIDs propagate in all directions throughout the day.

[84] The deposition of momentum on large scales from small-scale, variable convective sources in the lower atmosphere is not currently taken into account in large-scale GCMs, although parameterized orographic GWs are now being simulated in GCMs [Miyoshi and Fujiwara, 2008; Yiğit et al., 2009]. Thus, the global-scale energy and momentum budgets from GWs excited by deep convective sources are currently unknown. Near the mesopause, the horizontal deposition of momentum reverses the jets and drives the mesosphere away from radiative equilibrium [e.g., Holton, 1983; Fritts and Alexander, 2003]. Although this paper focuses on a single deep convective plume, typical convective storms last for many hours, and contain many to hundreds of deep convective plumes. Because each convective plume results in the creation of a “mean” neutral horizontal wind perturbation in the region of the body force which lasts for ~ 4 h, the combined “mean” neutral wind perturbations may cause a net global change of the neutral thermospheric winds and residual circulations that are highly variable in time, especially in the spring/summer/fall hemisphere. Yiğit et al. [2009] estimates possible thermospheric accelerations as large as ~ 150 m/s/day, with changes to the neutral wind circulation up to $z \sim 240$ km. Miyoshi and Fujiwara [2008] estimates time-varying variabilities of the zonal winds of ~ 100 – 200 m/s. Further global simulations are needed to answer this question.

[85] Although we only studied the dissipation of convectively generated GWs in this paper, the mechanism studied in this paper is a basic-physics mechanism that must be occurring in the thermosphere whenever waves dissipate there, regardless of their source. The source of GWs which can create thermospheric body forces include convection and shear. They also include the breaking of waves from wave flow over mountains, convection, and geostrophic adjustment in the lower atmosphere. Because lower atmospheric sources of GWs are prevalent and ubiquitous, the created large-scale secondary GWs in the thermosphere are expected to be ubiquitous and prevalent during geomagnetically active and quiet times alike. Because many wave sources likely contribute, the large-scale secondary GW spectrum and “mean” wind perturbations likely depend on season, LT, solar minimum/maximum, latitude, longitude, etc.

[86] The most powerful aspect of this new mechanism is that it results in the transfer of momentum from GWs with small scales and small phase speeds excited from small, localized sources in the lower atmosphere to GWs with large scales and large phase speeds that propagate globally in the thermosphere, and to large-scale, large “mean” neutral wind perturbations at $z \sim 120$ – 250 km. This mechanism is unrelated to geomagnetic activity. Note that the amplitudes of the secondary, large-scale GWs are somewhat smaller than the primary GWs which dissipate in the thermosphere. But because they have larger vertical wavelengths, they propagate to at least $z \sim 420$ km, far above the altitude where GWs from the lower atmosphere can penetrate (i.e., $z \lesssim 300$ km (see V2007)). Therefore, the excitation of large-scale, secondary GWs and LSTIDs from thermospheric body forces effectively extends the altitude range over which lower atmospheric sources can influence and create variability in the thermosphere and ionosphere.

[87] **Acknowledgments.** We would like to thank Pete Stamus and Fernando São Sabbas for the infrared images in Figure 1. We would like to thank Art Richmond for helpful comments. This research was supported by NASA contract NNH07CC81C and NSF grant ATM-0537311.

[88] Amitava Bhattacharjee thanks the reviewers for their assistance in evaluating this paper.

References

- Alexander, M. J., J. R. Holton, and D. R. Durran (1995), The gravity wave response above deep convection in a squall line simulation, *J. Atmos. Sci.*, *52*, 2212–2226.
- Andrews, D. G., J. R. Holton, and C. B. Leovy (1987), *Middle Atmosphere Dynamics*, Academic, Orlando, Fla.
- Bauer, S. J. (1958), An apparent ionospheric response to the passage of hurricanes, *J. Geophys. Res.*, *63*, 265–269.
- Beres, J. H. (2004), Gravity wave generation by a three-dimensional thermal forcing, *J. Atmos. Sci.*, *61*, 1805–1815.
- Bishop, R., N. Aponte, G. D. Earle, M. Sulzer, M. Larsen, and G. Peng (2006), Arecibo observations of ionospheric perturbations associated with the passage of tropical storm Odette, *J. Geophys. Res.*, *111*(A11), A11320, doi:10.1029/2006JA011668.
- Bluestein, H. B. (1993), *Synoptic-Dynamic Meteorology in Midlatitudes*, vol. II, *Observations and Theory of Weather Systems*, p. 444, Oxford Univ. Press, New York.
- Bluestein, H. B., E. W. McCaul Jr., G. P. Byrd, and G. R. Woodall (1988), Mobile sounding observations of a tornadic storm near the dryline: The Canadian, Texas storm of 7 May 1986, *Mon. Weather Rev.*, *116*, 1790–1804.
- Blumen, W. (1972), Geostrophic adjustment, *Rev. Geophys. Space Phys.*, *10*, 485–528.
- Bruinsma, S. L., and J. M. Forbes (2008), Medium- to large-scale density variability as observed by CHAMP, *Space Weather*, *6*, S08002, doi:10.1029/2008SW000411.
- Bühler, O., M. E. McIntyre, and J. F. Scinocca (1999), On shear-generated gravity waves that reach the mesosphere. Part I: wave generation, *J. Atmos. Sci.*, *56*, 3749–3763.
- Cowling, D. H., H. D. Webb, and K. C. Yeh (1971), Group rays of internal gravity waves in a wind-stratified atmosphere, *J. Geophys. Res.*, *76*, 213–220.
- Crowley, G., T. B. Jones, and J. R. Dudeney (1987), Comparison of short period TID morphologies in Antarctica during geomagnetically quiet and active intervals, *J. Atmos. Terr. Phys.*, *49*, 1155–1162.
- Del Genio, A. D., and G. Schubert (1979), Gravity wave propagation in a diffusively separated atmosphere with height-dependent collision frequencies, *J. Geophys. Res.*, *84*, 4371–4378.
- Dickinson, R. E. (1969), Propagators of atmospheric motions: 1. Excitation by point impulses, *Rev. Geophys.*, *7*, 483–538.
- Earle, G. D., A. M. Musumba, and S. L. Vadas (2008), Satellite-based measurements of gravity wave-induced midlatitude plasma density perturbations, *J. Geophys. Res.*, *113*, A03303, doi:10.1029/2007JA012766.
- Forbes, J., F. Marcos, and F. Kamalabadi (1995), Wave structures in lower thermosphere density from satellite electrostatic triaxial accelerometer measurements, *J. Geophys. Res.*, *100*(A8), 14,693–14,701.
- Francis, S. H. (1973), Acoustic-gravity modes and large-scale traveling ionospheric disturbances of a realistic dissipative atmosphere, *J. Geophys. Res.*, *78*, 2278–2301.
- Fritts, D. C., and M. J. Alexander (2003), Gravity wave dynamics and effects in the middle atmosphere, *Rev. Geophys.*, *41*(1), 1003, doi:10.1029/2001RG000106.
- Fritts, D. C., and Z. Luo (1992), Gravity wave excitation by geostrophic adjustment of the jet stream, Part I: Two-dimensional forcing, *J. Atmos. Sci.*, *49*, 681–697.
- Fritts, D. C., and S. L. Vadas (2008), Gravity wave penetration into the thermosphere: Sensitivity to solar cycle variations and mean winds, *Ann. Geophys.*, *26*, 3841–3861.
- Georges, T. M. (1968), HF doppler studies of traveling ionospheric disturbances, *J. Atmos. Terr. Phys.*, *30*, 735–746.
- Gerrard, A. J., T. J. Kane, S. D. Eckermann, and J. P. Thayer (2004), Gravity waves and mesospheric clouds in the summer middle atmosphere: A comparison of lidar measurements and ray modeling of gravity waves over Sondrestrom, Greenland, *J. Geophys. Res.*, *109*, D10103, doi:10.1029/2002JD002783.
- Gossard, E. E., and W. H. Hooke (1975), *Waves in the Atmosphere*, 456 pp., Elsevier Sci., Amsterdam.
- Hajkowicz, L. A. (1990), A global study of large scale travelling ionospheric disturbances (TIDs) following a step-like onset of auroral substorms in both hemispheres, *Planet. Space Sci.*, *38*, 913–923.
- Hajkowicz, L. A. (1991), Auroral electrojet effect on the global occurrence pattern of large scale travelling ionospheric disturbances, *Planet. Space Sci.*, *39*, 1189–1196.
- Hecht, J. H., S. Kovalam, P. T. May, G. Mills, R. A. Vincent, R. L. Walterscheid, and J. Woithe (2004), Airglow imager observations of atmospheric gravity waves at Alice Springs and Adelaide, Australia during the Darwin Area Wave Experiment (DAWEX), *J. Geophys. Res.*, *109*, D20S05, doi:10.1029/2004JD004697.
- Hedin, A. E., and H. G. Mayr (1987), Characteristics of wavelike fluctuations in Dynamics Explorer neutral composition data, *J. Geophys. Res.*, *92*, 11,159–11,172.
- Hines, C. O. (1960), Internal atmospheric gravity waves at ionospheric heights, *Can. J. Phys.*, *38*, 1441–1481.
- Hines, C. O. (1967), On the nature of traveling ionospheric disturbances launched by low-altitude nuclear explosions, *J. Geophys. Res.*, *72*, 1877–1882.
- Hines, C. O. (1972), Momentum deposition by atmospheric waves, and its effects on thermospheric circulation, *Space Res.*, *12*, 1157–1161.
- Hines, C. O., and W. H. Hooke (1970), Discussion of ionization effects on the propagation of acoustic-gravity waves in the ionosphere, *J. Geophys. Res.*, *75*, 2563–2568.
- Hines, C. O., and C. A. Reddy (1967), On the propagation of atmospheric gravity waves through regions of wind shear, *J. Geophys. Res.*, *72*, 1015–1034.
- Hocke, K., and K. Schlegel (1996), A review of atmospheric gravity waves and traveling ionospheric disturbances: 1982–1995, *Ann. Geophys.*, *14*, 917–940.
- Hocke, K., and T. Tsuda (2001), Gravity waves and ionospheric irregularities over tropical convection zones observed by GPS/MET radio occultation, *Geophys. Res. Lett.*, *28*, 2815–2818.
- Holton, J. R. (1983), The influence of gravity wave breaking on the general circulation of the middle atmosphere, *J. Atmos. Sci.*, *40*, 2497–2507.
- Holton, J. R., and M. J. Alexander (1999), Gravity waves in the mesosphere generated by tropospheric convection, *Tellus, Ser. B*, *51*, 45–58.
- Horinouchi, T., T. Nakamura, and J. Kosaka (2002), Convectively generated mesoscale gravity waves simulated throughout the middle atmosphere, *Geophys. Res. Lett.*, *29*(21), 2007, doi:10.1029/2002GL016069.
- Hung, R. J., and J. P. Kuo (1978), Ionospheric observation of gravity-waves associated with hurricane Eloise, *J. Geophys.*, *45*, 67–80.
- Hung, R. J., and R. E. Smith (1978), Ray tracing of gravity waves as a possible warning system for tornadic storms and hurricanes, *J. Appl. Meteorol.*, *17*, 3–11.
- Hung, R. J., T. Phan, and R. E. Smith (1978), Observations of gravity waves during the extreme tornado outbreak of 3 April 1974, *J. Atmos. Terr. Phys.*, *40*, 831–843.
- Jones, W. (1969), Ray tracing for internal gravity waves, *J. Geophys. Res.*, *74*(8), 2028–2033.
- Kelley, M. C. (1997), In situ ionospheric observations of severe weather-related gravity waves and associated small-scale plasma structure, *J. Geophys. Res.*, *102*, 329–335.
- Kirchengast, G., K. Hocke, and K. Schlegel (1996), The gravity wave-TID relationship: Insight via theoretical model-EISCAT data comparison, *J. Atmos. Terr. Phys.*, *58*, 233–243.
- Klostermeyer, J. (1972), Numerical calculation of gravity wave propagation in a realistic thermosphere, *J. Atmos. Terr. Phys.*, *34*, 765–774.
- Kundu, P. (1990), *Fluid Dynamics*, 638 pp., Academic, San Diego, Calif.
- Lane, T. P., M. J. Reeder, and T. L. Clark (2001), Numerical modeling of gravity waves generated by deep tropical convection, *J. Atmos. Sci.*, *58*, 1249–1274.
- Lane, T. P., R. D. Sharman, T. L. Clark, and H.-M. Hsu (2003), An investigation of turbulence generation mechanisms above deep convection, *J. Atmos. Sci.*, *60*, 1297–1321.
- Lighthill, J. (1978), *Waves in Fluids*, 504 pp., Cambridge Univ. Press, Cambridge, U. K.
- Lu, G., A. D. Richmond, R. G. Roble, and B. A. Emery (2001), Coexistence of ionospheric positive and negative storm phases under northern winter conditions: A case study, *J. Geophys. Res.*, *106*(A11), 24,493–24,504.
- Luo, Z., and D. C. Fritts (1993), Gravity wave excitation by geostrophic adjustment of the jet stream, Part II: Three-dimensional forcing, *J. Atmos. Sci.*, *50*, 104–115.
- Maeda, S. (1985), Numerical solutions of the coupled equations for acoustic-gravity waves in the upper thermosphere, *J. Atmos. Terr. Phys.*, *47*, 965–972.
- Maeda, S., and S. Handa (1980), Transmission of large-scale TIDs in the ionospheric F2-region, *J. Atmos. Terr. Phys.*, *42*, 853–859.
- Marks, C. J., and S. D. Eckermann (1995), A three-dimensional nonhydrostatic ray-tracing model for gravity waves: Formulation and preliminary results for the middle atmosphere, *J. Atmos. Sci.*, *52*, 1959–1984.
- Mayr, H. G., I. Harris, F. A. Herrero, N. W. Spencer, F. Varosi, and W. D. Pesnell (1990), Thermospheric gravity waves: observations and interpretation using the transfer function model (TEM), *Space Sci. Rev.*, *54*, 297–375.

- Menzel, W. P., and J. F. W. Purdom (1994), Introducing GOES-I: The first of a new generation of geostationary operational environmental satellites, *Bull. Am. Meteorol. Soc.*, *75*, 757–781.
- Miyoshi, Y., and H. Fujiwara (2008), Gravity waves in the thermosphere simulated by a general circulation model, *J. Geophys. Res.*, *113*, D01101, doi:10.1029/2007JD008874.
- Piani, C., D. Durran, M. J. Alexander, and J. R. Holton (2000), A numerical study of three dimensional gravity waves triggered by deep tropical convection, *J. Atmos. Sci.*, *57*, 3689–3702.
- Pitteway, M. L. V., and C. O. Hines (1963), The viscous damping of atmospheric gravity waves, *Can. J. Phys.*, *41*, 1935–1948.
- Richmond, A. D. (1978), Gravity wave generation, propagation, and dissipation in the thermosphere, *J. Geophys. Res.*, *83*, 4131–4145.
- Roble, R. G. (1995), Energetics of the mesosphere and thermosphere, in *The Upper Mesosphere and Lower Thermosphere: A Review of Experiment and Theory*, *Geophys. Monogr. Ser.*, vol. 87, edited by R. M. Johnson and T. L. Killeen, pp. 1–21, AGU, Washington, D. C.
- Roble, R. G. (2000), On the feasibility of developing a global atmospheric model extending from the ground to the exosphere, in *Atmospheric Science Across the Stratopause*, *Geophys. Monogr. Ser.*, vol. 123, edited by D. E. Siskind, S. D. Eckermann, and M. E. Summers, pp. 53–67, AGU, Washington, D. C.
- Roble, R. G., and E. C. Ridley (1994), A thermosphere-ionosphere-mesosphere-electrodynamics general circulation model (TIME-GCM): Equinox solar cycle minimum simulations (30–500 km), *Geophys. Res. Lett.*, *21*, 417–420.
- Röttger, J. (1977), Travelling disturbances in the equatorial ionosphere and their association with penetrative cumulus convection, *J. Atmos. Terr. Phys.*, *39*, 987–998.
- Schlegel, K. (1986), The study of tides and gravity waves with the help of field-aligned velocities measured by EISCAT, *J. Atmos. Terr. Phys.*, *48*, 879–886.
- Sharadze, Z. S., N. D. Kvadze, Z. L. Liyadze, and N. V. Mosahvili (1986), Travelling ionospheric disturbances and the appearance of F scattering in the midlatitude ionosphere, *Geomagn. Aeron.*, *26*, 117–119.
- Shibata, T. (1986), Two classes of medium-scale traveling ionospheric disturbances observed by an HF Doppler array, *J. Geomagn. Geoelectr.*, *38*, 779–796.
- Shibata, T., and K. Schlegel (1993), Vertical structure of AGW associated ionospheric fluctuations in the E- and lower F-region observed with EISCAT—A case study, *J. Atmos. Terr. Phys.*, *55*, 739–749.
- Shiokawa, K., Y. Otsuka, and T. Ogawa (2006), Quasiperiodic southward moving waves in 630-nm airglow images in the equatorial thermosphere, *J. Geophys. Res.*, *111*, A06301, doi:10.1029/2005JA011406.
- Stull, R. B. (1976), Internal gravity waves generated by penetrative convection, *J. Atmos. Sci.*, *33*, 1279–1286.
- Tsugawa, T., A. Saito, Y. Otsuka, and M. Yamamoto (2003), Damping of large-scale traveling ionospheric disturbances detected with GPS networks during the geomagnetic storm, *J. Geophys. Res.*, *108*(A3), 1127, doi:10.1029/2002JA009433.
- Vadas, S. L. (2007), Horizontal and vertical propagation and dissipation of gravity waves in the thermosphere from lower atmospheric and thermospheric sources, *J. Geophys. Res.*, *112*, A06305, doi:10.1029/2006JA011845.
- Vadas, S. L., and D. C. Fritts (2001), Gravity wave radiation and mean responses to local body forces in the atmosphere, *J. Atmos. Sci.*, *58*, 2249–2279.
- Vadas, S. L., and D. C. Fritts (2004), Thermospheric responses to gravity waves arising from mesoscale convective complexes, *J. Atmos. Sol. Terr. Phys.*, *66*, 781–804.
- Vadas, S. L., and D. C. Fritts (2005), Thermospheric responses to gravity waves: Influences of increasing viscosity and thermal diffusivity, *J. Geophys. Res.*, *110*, D15103, doi:10.1029/2004JD005574.
- Vadas, S. L., and D. C. Fritts (2006), Influence of solar variability on gravity wave structure and dissipation in the thermosphere from tropospheric convection, *J. Geophys. Res.*, *111*, A10S12, doi:10.1029/2005JA011510.
- Vadas, S. L., and D. C. Fritts (2009), Reconstruction of the gravity wave field from convective plumes via ray tracing, *Ann. Geophys.*, *27*, 147–177.
- Vadas, S. L., and M. J. Nicolls (2009), Temporal evolution of neutral, thermospheric winds and plasma response using PFISR measurements of gravity waves, *J. Atmos. Sol. Terr. Phys.*, *71*, 740–770.
- Vadas, S. L., D. C. Fritts, and M. J. Alexander (2003), Mechanism for the generation of secondary waves in wave breaking regions, *J. Atmos. Sci.*, *60*, 194–214.
- Vadas, S. L., M. J. Taylor, P.-D. Pautet, P. A. Stamus, D. C. Fritts, H.-L. Liu, F. T. Sao Sabbas, V. T. Rampinelli, P. Batista, and H. Takahashi (2009a), Convection: the likely source of the medium-scale gravity waves observed in the OH airglow layer near Brasilia, Brazil, during the SpreadFEx campaign, *Ann. Geophys.*, *27*, 231–259.
- Vadas, S. L., J. Yue, C.-Y. She, P. A. Stamus, and A. Liu (2009b), A model study of the effects of winds on concentric rings of gravity waves from a convective plume near Fort Collins on 11 May 2004, *J. Geophys. Res.*, *114*, D06103, doi:10.1029/2008JD010753.
- Waldock, J. A., and T. B. Jones (1984), The effects of neutral winds on the propagation of medium-scale atmospheric gravity waves at mid-latitudes, *J. Atmos. Terr. Phys.*, *46*, 217–231.
- Waldock, J. A., and T. B. Jones (1986), HF doppler observations of medium-scale travelling ionospheric disturbances at mid-latitudes, *J. Atmos. Terr. Phys.*, *48*, 245–260.
- Waldock, J. A., and T. B. Jones (1987), Source regions of medium scale travelling ionospheric disturbances observed at mid-latitudes, *J. Atmos. Terr. Phys.*, *49*, 105–114.
- Walker, G. O., Y. W. Wong, H. K. Ma, T. Kikuchi, K. Nozaki, Y. N. Hung, and V. Badillo (1988), Propagating ionospheric waves observed throughout East Asia during the WAGS October 1985 campaign, *Radio Sci.*, *23*, 867–878.
- Walterscheid, R. L., and D. J. Boucher Jr. (1984), A simple model of the transient response of the thermosphere to impulsive forcing, *J. Atmos. Sci.*, *41*, 1062–1072.
- Walterscheid, R. L., G. Schubert, and D. G. Brinkman (2001), Small-scale gravity waves in the upper mesosphere and lower thermosphere generated by deep tropical convection, *J. Geophys. Res.*, *106*(D23), 31,825–31,832.
- Yeh, K. C., C. H. Liu, and M. Y. Youakim (1975), Attenuation of internal gravity waves in model atmospheres, *Ann. Geophys.*, *31*, 321–328.
- Yigit, E., A. D. Aylward, and A. S. Medvedev (2008), Parameterization of the effects of vertically propagating gravity waves for thermosphere general circulation models: Sensitivity study, *J. Geophys. Res.*, *113*, D19106, doi:10.1029/2008JD010135.
- Yigit, E., A. S. Medvedev, A. D. Aylward, P. Hartogh, and M. J. Harris (2009), Modeling the effects of gravity wave momentum deposition on the general circulation above the turbopause, *J. Geophys. Res.*, *114*, D07101, doi:10.1029/2008JD011132.
- Zhu, X., and J. R. Holton (1987), Mean fields induced by local gravity-wave forcing in the middle atmosphere, *J. Atmos. Sci.*, *44*, 620–630.

H. Liu, High Altitude Observatory, National Center for Atmospheric Research, P.O. Box 3000, Boulder, CO 80305, USA.

S. L. Vadas, CoRA Division, NorthWest Research Associates, 3380 Mitchell Lane, Boulder, CO 80301, USA. (vasha@cora.nwra.com)